

Master's thesis

NTNU
Norwegian University of Science and Technology
Faculty of Natural Sciences
Department of Physics

Herman Martens Meyer

Recognising sub-surface turbulence via light reflected from a free surface

Master's thesis in Applied Physics and Mathematics

Supervisor: Simen Ådnøy Ellingsen

June 2025



NTNU

Norwegian University of
Science and Technology

Herman Martens Meyer

Recognising sub-surface turbulence via light reflected from a free surface

Master's thesis in Applied Physics and Mathematics
Supervisor: Simen Ådnøy Ellingsen
June 2025

Norwegian University of Science and Technology
Faculty of Natural Sciences
Department of Physics



Norwegian University of
Science and Technology

Abstract

The interplay between turbulent motion and free surfaces plays a vital role in the exchange of heat and gas through the air-water interface. Despite this, research into these interactions remains limited and experiments require expensive facilities and substantial processing power. This proof-of-concept study investigates a straightforward, low-cost, and widely accessible imaging approach that utilises optical reflections from a free surface and a wavelet-based computer vision method to detect and track surface-attached vortices.

The experimental data analysed in this project were collected in a recirculating open water channel with an active turbulence grid. The three simultaneous measurements included stereoscopic particle image velocimetry at a depth of 10 mm, Fourier-transform profilometry of the surface, and a recording of the reflections cast onto a projector screen on the ceiling by the fluorescently dyed free surface illuminated by a projector. The primary objectives were to detect and track the imprints of surface-attached vortices, known as dimples, using reflection data and assess their correlation with sub-surface vorticity. Furthermore, the reflection-based tracking method is compared with dimple tracking using direct surface measurements from profilometry.

Using a two-dimensional continuous wavelet transform combined with shape filtering, dimples are reliably detected in the reflections. A novel advection-based tracking scheme mitigates false positives by filtering out short-lived detections, leveraging the fact that surface-attached vortices are typically long-lived. Sub-surface vortices are identified in the measured velocity field using the λ_2 criterion of Jeong and Hussain (*J. Fluid Mech.*, 1995). The match ratio analysis indicates that sub-surface vortices are significantly more likely to be located beneath a detected dimple than beneath a randomly placed surface point. While profilometry achieves a higher match ratio overall, it detects fewer dimples than the reflection-based method.

Moreover, the number of detected dimples from surface reflections shows a clear correlation with the mean square horizontal divergence in the sub-surface flow, even slightly higher than the correlation obtained using profilometry-based detections. The near-surface horizontal divergence is closely tied to the local rate of gas transfer between air and water. These findings demonstrate that non-contact optical methods can provide insight into the near-surface turbulence, thereby opening pathways to the affordable monitoring of gas-transfer-relevant processes. Future work will include refining the computer vision methodology, determining the optimal distance between the free surface and the projector screen for reflection patterns, and extending this approach to other relevant surface features.

Sammendrag

Samspillet mellom turbulens og frie overflater spiller en viktig rolle for hvordan gass og varme utveksles mellom luft og vann. Forskning på disse interaksjonene er begrenset, og eksperimenter krever dyre fasiliteter og mye beregningskraft. Dette demonstrasjonsstudiet utforsker en enkel, billig og tilgjengelig avbildningsmetode som bruker de optiske refleksjonene fra en vannoverflate og en Wavelet-basert maskinsynsmetode til å identifisere og følge virvler festet til overflaten.

De eksperimentelle dataene analysert i dette prosjektet ble samlet inn i den åpne vannkanalen ved NTNU, Trondheim, der turbulensen ble generert av et aktivt gitter, og inkluderer simultane målinger av stereoskopisk partikelbildemåling av hastighetsfelt på 10 mm dybde, Fourier-transformasjonsprofilometri av overflaten, samt et opptak av refleksjonene i taket, fra overflaten med fluorescerende fargestoff belyst av en projektor. Målene med prosjektet var å detektere og følge de optiske signaturene fra virvler festet til overflaten, kalt dimpler, og undersøke deres korrelasjon med virvler under overflaten. Denne metoden med refleksjonsbasert deteksjon blir evaluert mot direkte overflatemåling med profilometri.

Ved å bruke en to-dimensjonal kontinuerlig Wavelet-transformasjon kombinert med fasongfiltrering blir dimpler detektert i refleksjonsdataen på en pålitelig måte. Et adveksjonsbasert sporingsssystem minimerer støy og deteksjon av falske positive ved å ekskludere refleksjonene med kortest levetid, ettersom overflatefestede virvler typisk har lang levetid. Virvler under overflaten blir detektert med λ_2 -kriteriet til Jeong og Hussain (*J. Fluid Mech.*, 1995) og analysen av treffprosenten, som sammenligner hvor mange refleksjoner med en virvler under seg, viser at det er vesentlig høyere treffprosent fra refleksjonene enn for et tilfeldig søk fra overflaten. Selv om profilometrien oppnår en høyere treffprosent, finner den ikke like mange dimpler som finnes i refleksjonsdataen.

Videre viser antall refleksjoner funnet gjennom overflaterefleksjonene en klar korrelasjon med gjennomsnittlig horisontal divergens under overflaten, tilsvarende korrelasjon som finnes med profilometridataen. Horisontal divergens nært overflaten er vist å ha en tett sammenheng med den lokalen gassutvekslingsraten mellom luft og vann. Disse funnene demonstrerer at kontaktløse optiske metoder kan gi direkte innsikt i turbulensen nær en fri overflate og åpne for mer kostnadseffektiv overvåkning av gassutvekslingsrelevante prosesser i både felt og laboratorium. Fremtidig arbeid kan innebære videreutvikling av maskinsynsmetoden, bestemme optimal avstand til detektor for refleksjonsbildene og å utvide denne metoden til å inkludere andre overflatefenomener.

Preface

I would like to express my heartfelt thanks to my supervisor, Simen Å. Ellingsen, for invaluable advice, encouragement and for sparking an interest in this fascinating field. Also, a special thanks for pointing out that I resemble a young Bryan Adams, and by that logic, apparently have a bright future ahead.

Warm thanks also go to Amélie Ferran and Ali Semati for conducting experiments, and to Omer M. Babiker for being such an invaluable resource when it comes to Wavelets and dimple detection. Thank you all for politely answering all my many (stupid) questions. Finally, thank you to the rest of the Ellingsen research group for providing feedback and cake at the biweekly meetings. You all have made this past year a rewarding experience.

And finally, I would like to provide my sincere apologies to my girlfriend, who can no longer walk along a river without being on the receiving end of a steady stream of facts and fascination about turbulence and free surfaces.

Contents

Abstract	i
Sammendrag	iii
Preface	v
Contents	vii
Nomenclature	viii
1 Introduction	1
1.1 Motivation	1
1.2 State of the art	3
1.3 Research gap	4
1.4 Objectives	5
1.5 Outline	5
1.6 A note to the reader	6
2 Theory	7
2.1 Turbulence	7
2.1.1 The energy cascade and the scales of turbulence	8
2.1.2 Turbulent statistics	9
2.2 Surface dynamics and imprints in free-surface turbulent flows	11
2.3 Fundamentals of vorticity and vortex dynamics	13
2.4 The surface layer in free-surface turbulent flows	16
2.5 The optics of surface reflections	18
3 Methods	21
3.1 Experimental setup	21
3.1.1 Laser Doppler velocimetry	22
3.1.2 Post-processing and calibration of reflection video	23
3.2 Wavelet analysis	24
3.2.1 Two-dimensional wavelet analysis	25
3.3 Computer vision technique	25
3.3.1 Dimple tracking	27
3.4 Vortex core detection in the sub-surface flow region	28
3.5 Surface and sub-surface correspondence metrics	29

4 Results and Discussion	31
4.1 Flow case and turbulent parameters	31
4.2 Parameter tuning for dimple detection and sub-surface vortices	32
4.2.1 Dimple detection and tracking parameters	32
4.2.2 Vortex core detection	34
4.3 Surface reflection detections as imprints of sub-surface vortices	36
4.3.1 Impact of sorting sub-surface vortices by lifetime	40
4.4 Comparison of surface reflection dimple detection with direct profilometry measurements	42
4.5 Dimple detections and sub-surface horizontal divergence	45
4.6 Outlook and future directions	49
5 Conclusions	51
References	53
Appendices:	57
A Code availability	57

Nomenclature

Abbreviations

FTP	Fourier transform profilometry
LDV	Laser Doppler velocimetry
PIV	Particle image velocimetry
SPIV	Stereoscopic particle image velocimetry

Non-dimensional numbers

Fr	Froude number
Re	Reynolds number
We	Weber number

Symbols

α	Angle of attached vorticity
b	Constant for translating mother wavelet
D_h	Horizontal divergence
D_V	Number of detections with a vortex below
D_N	Number of detections without a vortex below
Δ	Dimple advection distance
ϵ	Dissipation
ϵ_{ijk}	Levi-Civita tensor
f	Signal analysed with wavelet analysis
f_i	External forcing
k	Turbulent kinetic energy
L	Characteristic turbulent length scale (Brocchini and Peregrine, 2001)
L_∞	Integral length scale (Brocchini and Peregrine, 2001)
\mathcal{L}	Characteristic length scale

λ_2	Vector field determining vortex core locations
$\lambda_{2,\text{thr}}$	Threshold for vortex detection
\mathcal{M}	Match ratio
$\nabla_i(t)$	Identified dimple i after wavelet filtering and shape filtering
ν	Viscosity
ω	Vorticity
Ω	Anti-symmetric part of velocity gradient tensor
p	Pressure
$P[R_V]$	Probability of finding a vortex below an arbitrary surface position
$P[R_D]$	Probability of finding a dimple above an arbitrary sub-surface position
q	Characteristic turbulent velocity scale (Brocchini and Peregrine, 2001)
r_e	Error radius for dimple tracking
r_s	Search radius for comparing dimples and vortices
s	Wavelet scale
σ	Surface tension
\mathbf{S}	Symmetric part of velocity gradient tensor
\mathcal{S}	Solidity
t	Time
t_{\min}	Lifetime threshold for surface detections
$t_{\min,\text{subsurface}}$	Lifetime threshold for subsurface vortices
\mathcal{T}	Temperature
θ	Angle of rotation
u_i	Instantaneous velocity
u'_i	Velocity fluctuations
U_i	Mean velocity
\mathcal{U}	Characteristic velocity
V'	Small volume enclosing a section of a vortex tube
V_D	Number of vortices with a detection above
V_N	Number of vortices without a dimple above
\mathcal{V}	Vortex match ratio
ρ	Density
W_{thr}	Wavelet threshold
W	Wavelet transform
ψ	Wavelet basis function (mother wavelet)

Chapter 1

Introduction

This thesis is a proof-of-concept study investigating the remote sensing potential of tracking turbulent imprints on a free surface through surface reflections on a projector screen. The analysis uses measurements from a water channel experiment in which turbulence is generated using an active grid. The three simultaneous measurements include: stereoscopic particle image velocimetry (SPIV) at a depth $d = 10$ mm, Fourier transform profilometry (FTP) of the surface, and surface reflections on a projector screen. A schematic of the surface reflections is presented in Fig. 1.1 to show conceptually how this data is captured. More detailed descriptions of the full experimental setup are presented Section 3.1.

This work aims to develop and evaluate a wavelet-based computer vision method capable of identifying and tracking small-scale surface deformations, referred to as dimples, in the reflection plane. Dimples are the imprints on the surface of surface-attached vortices. These surface features are then correlated with sub-surface turbulent phenomena to further investigate the remote sensing potential of this method and its promising potential for estimating gas transfer rates through the air-water interface. This aligns with the ongoing research of the group with whom this project is being carried out in collaboration. The performance of this novel, non-intrusive sensing approach is benchmarked against direct surface measurements with profilometry.

The research questions addressed in this thesis are therefore as follows:

- Can small-scale deformations on a free surface be reliably identified and tracked through surface reflection patterns?
- To what extent do these detections correlate with sub-surface vortices and horizontal divergence?
- How does the robustness of detection via surface reflections compare to detection via direct surface elevation measurements using Fourier transform profilometry?

1.1 Motivation

Turbulence interacting with free surfaces plays a crucial role in regulating the exchange of gas and heat between water and the atmosphere, a process with

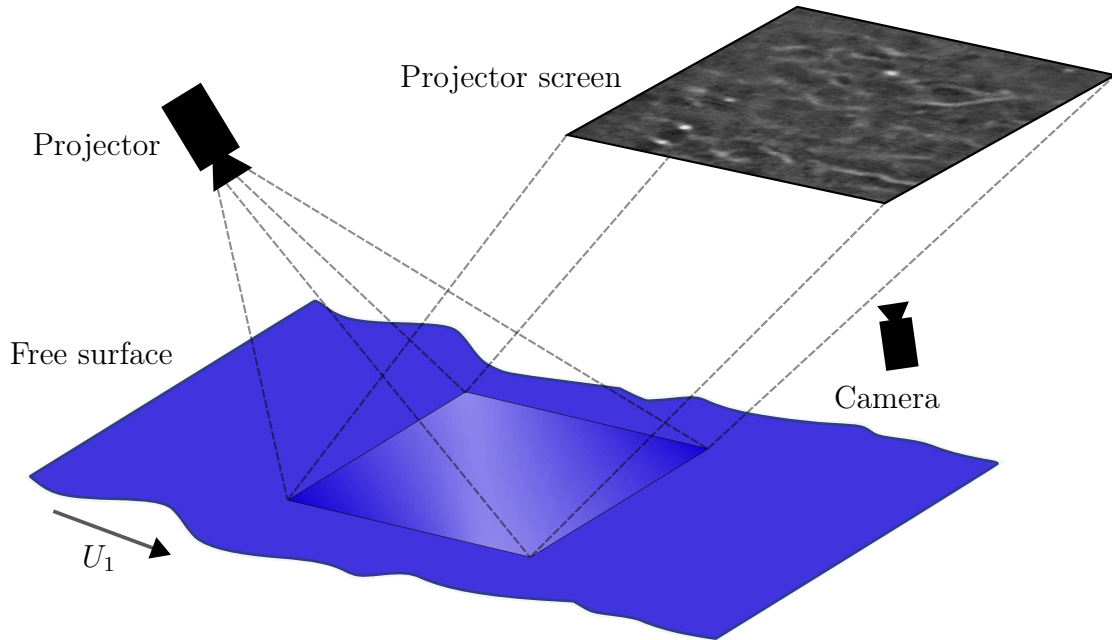


Figure 1.1: Conceptual schematic of surface reflection projections. A projector illuminates the free surface, and the light reflected from this surface is captured on a screen on the ceiling. The complete experimental setup is described in Section 3.1. The camera illustrates how these reflections are recorded on the screen from below. In this figure, the reflected pattern is placed above for illustrative purposes.

significant climate implications (Wanninkhof et al., 2009; D’Asaro, 2014). Rivers, where the structures investigated in this project are most often found, are vital to the Earth’s total carbon budget. The global river network emits comparable amounts of CO₂ as the total oceanic carbon uptake (Brinkerhoff et al., 2022). However, these numbers are highly uncertain (Rocher-Ros et al., 2019), and the physical process underlying this phenomenon is not yet fully understood, making research into quantifying and understanding the gas transfer rate essential. A typical river flow is illustrated in Fig. 1.2, where the different surface imprints have their unique connection with the sub-surface turbulence. This will be revisited in Chapter 2. Measuring the surface accurately over larger regions is a significant challenge. Although direct, *in situ* measurements offer precise local data, non-contact techniques can potentially cover greater areas at a reduced cost. The advancement in precise non-contact measurements could also unlock faster, better, and cheaper ways to investigate the intricate dynamics between turbulence and the free surface, possibly leading to a better understanding of this complex process.

The gas transfer rate through the air-water interface is linked to surface renewal processes. Recently, Li et al. (2025) has shown that the near-surface turbulence is the governing factor in determining the gas-transfer rates between air and water even in the presence of non-breaking waves. More specifically, this surface renewal process links to upwelling boils, and the vortices which attach to the surface tend to form at the edges of these boils (Banerjee, 1994). The detection of dimples at the surface thus offers an indirect observational link to the underlying gas-transfer processes, as recently shown by Babiker et al. (2023) using a wavelet-based

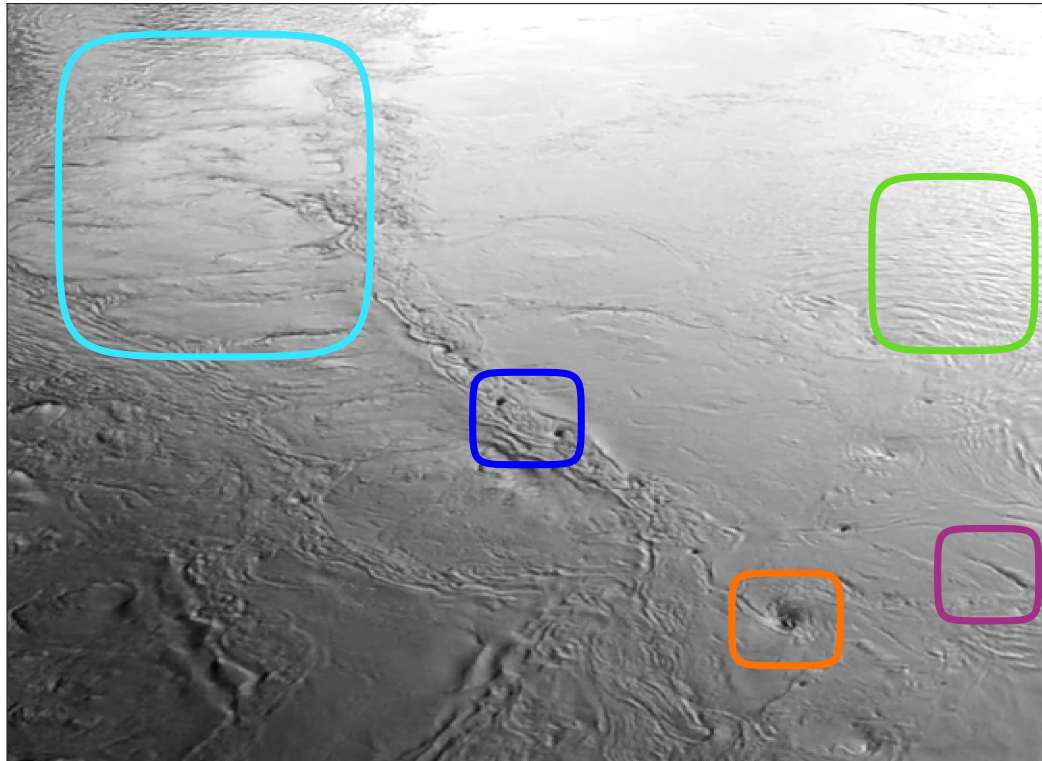


Figure 1.2: Surface deformation phenomena observed on the Nidelva river, including a portion of an upwelling boil (light blue), dimples (deep blue), vortex shedding from the bridge pillar (orange), capillary waves (green), and scars (purple). This figure is adapted from Martens Meyer (2024).

detection method. These methods effectively detect edges and localised features, such as dimples, which are circular and uniform in size.

More specifically, towards this project, linking the imprints of turbulence on a free surface to their sub-surface counterparts usually requires precise, direct measurements of the surface elevation profile. Investigating the qualitative relationship between the sub-surface velocity field and the surface reflection patterns is interesting from a physical perspective. A deeper understanding of this relationship could enable simpler and computationally cheaper approaches to infer flow characteristics from visual data, both in laboratory settings and in real-world applications.

Trying to obtain physical insight from a video of surface reflections aligns with the emerging concept often referred to as ‘GoPro physics’: the idea of capturing physical phenomena using readily available imaging tools, such as cameras, and extracting meaningful physical insights by processing this visual data computationally (Gao et al., 2025). In essence, the goal is to film a process of interest, analyse the footage using data-driven or physics-informed algorithms, and recover the underlying physical behaviour from the visual observations.

1.2 State of the art

This section reviews the current state of the art regarding free-surface turbulence, wavelet analysis, and their combined application. The aim is to identify current

research gaps and present the context of the research conducted, as well as the methods used in this project.

For the interaction of turbulence with a free surface, Brocchini and Peregrine (2001) provides a seminal contribution to understanding these phenomena. The comprehensive study investigates the behaviour of the free surface under different turbulent conditions. Although their discussion is heuristic due to a lack of experimental data, this serves as a strong foundation for future investigations and validation. The review of Muraro et al. (2021) expands on this and gathers information relevant for a better understanding of the link between the free surface and the underlying processes. Many studies are attempting to link sub-surface phenomena to free-surface imprints. Mandel et al. (2019) analyses the flow over submerged cylinders and the surface imprints created. The cylinders represent submerged vegetation and demonstrate how the vortex properties measured at the surface can be linked to the river bed topography and measurements in the bulk flow. Muraro et al. (2021) presents more examples of studies related to the interaction between turbulent motion and free surfaces.

Wavelet analysis provides a powerful tool for investigating complex signals arising from multi-scale processes, such as turbulence (Brunton and Kutz, 2019, p. 85). Farge (1992) provides a thorough overview of the application of wavelets to turbulence problems. However, wavelets have a wide range of applications in other complex signal problems, such as Wang and Lu (2010), which investigates two-dimensional wavelets on meteorological data. Wavelet analysis also has a broad range of applications in finance (In and Kim, 2012). Returning to fluid mechanics applications, Dolcetti and Nava (2019) demonstrated that, using wavelet analysis, it is possible to estimate key flow parameters of a turbulent flow under a free surface using only three point sensors.

Wavelets are highly efficient in highlighting edges (Grossmann, 1988), making them a powerful tool in object detection. This capability has led to their integration into YOLO (You Only Look Once) models for enhancing object detection performance (Y. Su et al., 2024). Related to flow problems, Gakhar et al. (2022) used the surface slope field and a wavelet-based method to identify the surface expressions of underwater features, and Schram et al. (2004) uses a wavelet-based method to detect coherent eddies in a backward facing step flow. More specifically, regarding the work conducted in this project, Babiker et al. (2023) employed direct numerical simulations (DNS) of turbulence interacting with a free surface and utilised a wavelet-based method to detect and track surface-attached vortices. They found that the number of these vortices correlates with surface divergence. As a development of this work, Aarnes et al. (2025) used the same wavelet-based method to show and quantify that the sub-surface vorticity field connects to specific surface features.

1.3 Research gap

This project aims to determine whether the same connections between the surface and sub-surface domains can be explored using a non-contact 'GoPro physics' wavelet-based approach, as with direct measurements and methods that require substantial data processing. Although multiple studies have investigated the inter-

action between turbulence and the free surface above, the qualitative relationship remains relatively unexplored. Proposing a simple, transparent, and effective way to analyse this connection could lead to more accessible investigations and possibly contribute to a deeper understanding of this complex phenomenon.

1.4 Objectives

The primary objective, which enables addressing the first research question, is to implement and develop a reliable method for detecting and tracking the dimples observed in the surface reflections using wavelet analysis and guided by key physical principles. Although based on the approach used by Babiker et al. (2023) and Aarnes et al. (2025), the method needs to be extended to a problem including a mean flow and the specific demands of working with such indirect measurements.

Whereas powerful machine learning methods are available and perform well at object detection and likely applicable to the present study, a key aim was to demonstrate how an explainable and simple approach could be as powerful in analysing such complex processes. Importantly, such a method makes it easier to interpret the results in light of the underlying physics.

To establish a realistic basis for comparison and effectively address the two final research questions, the data for the surface reflections required post-processing and calibration, along with an analysis of the associated uncertainties. Additionally, vortices in the sub-surface flow field need to be defined and analysed to compare surface structures with the underlying turbulence. To enable a valid comparison with the results from other studies, an appropriate metric specific to the current method and data had to be defined, along with determining the turbulent parameters of the flow in question. After the proper calibration, the comparison between structures detected in the surface reflections and the sub-surface vortices will look like that presented in Fig. 1.3, where the reflection plane is mapped onto its physical surface coordinates.

Finally, as this is primarily a proof-of-concept study, the final objective is to identify and evaluate how this method can be further developed and applied in future experimental studies and applications.

1.5 Outline

The rest of this thesis is organised as follows. In Chapter 2, a general introduction to turbulence is provided before focussing on how turbulent motion below the surface imprints on the surface, along with an introduction to the dynamics of the near-surface region. Chapter 3 describes the experimental setup used to acquire the data for this study, along with an overview of the theoretical foundations of wavelet analysis and the wavelet-based computer vision algorithm developed for this work. The definition and identification of sub-surface vortices are also introduced in this chapter. The results obtained using the proposed computer vision method are presented and discussed in Chapter 4, with particular emphasis on how they address the research questions. Finally, conclusions are drawn in Chapter 5.

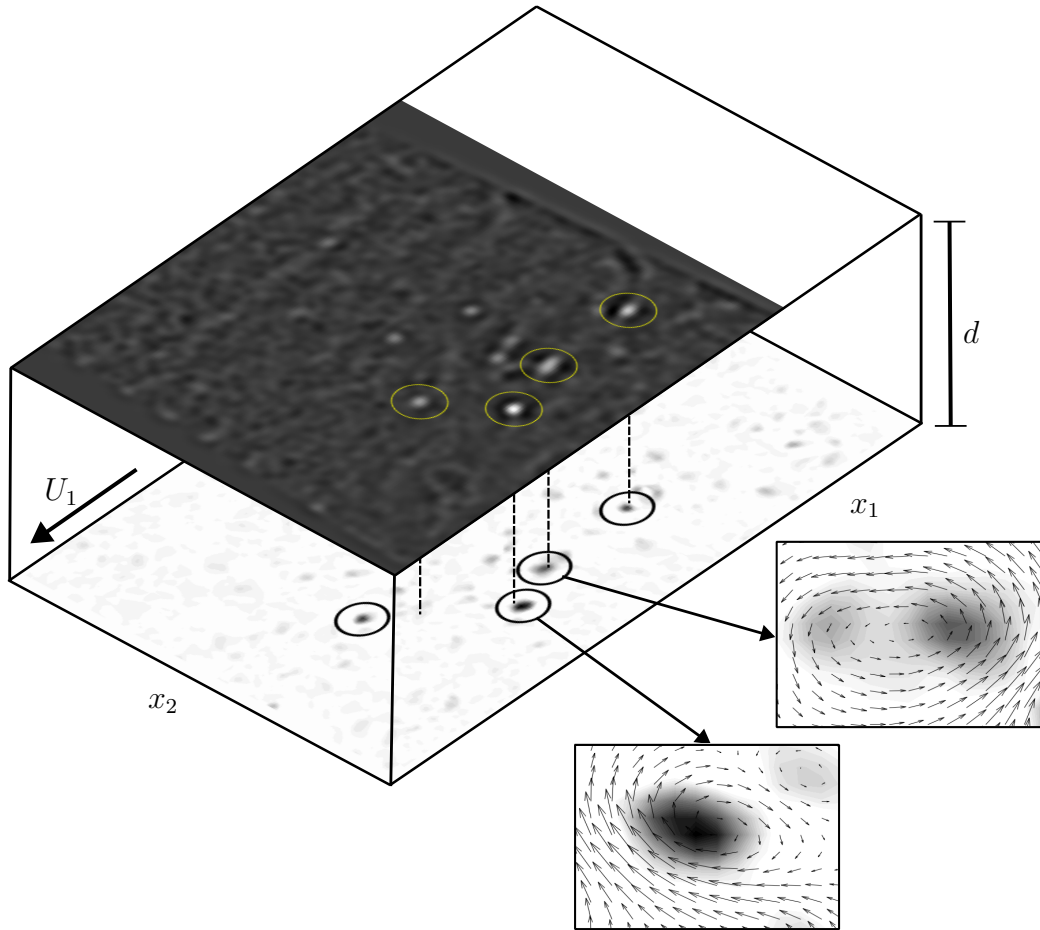


Figure 1.3: Conceptual schematic comparing surface and sub-surface detections at a single timestep. **Top plane:** The free surface, seen via its reflection on the ceiling, re-positioned to its true physical location. Yellow circles indicate detections of surface dimples. **Bottom plane:** A projection of these detected dimples into the sub-surface region at a depth d as the dashed lines. Black circles denote vortices identified using the λ_2 criterion. The insets show a detailed view of the local velocity field surrounding two vortices.

1.6 A note to the reader

This thesis is partially building on the specialisation project of Martens Meyer (2024). Although the objectives, methods and results differ, the underlying motivation and theoretical framework will share similarities. This thesis can be considered a continuation and expansion of the earlier project. More specifically, Sections 2.1 and 2.2 are present in both works, although revised and expanded for this report.

Chapter 2

Theory

This chapter aims to establish the theoretical foundation needed for understanding the fluid flow phenomena investigated in this thesis. Initially, a general introduction to turbulence is provided in Section 2.1, followed by the key terminology necessary for a deeper exploration of free-surface turbulence. This exploration focuses on how turbulent motion underneath the surface impacts the surface in Section 2.2 and vice versa in Section 2.4, as well as how vorticity and vortex motion interact and evolve in Section 2.3. Finally, the chapter presents the simple optical principles underlying the use of surface reflections to identify and analyse surface features in Section 2.5.

2.1 Turbulence

Turbulence remains one of the most significant unsolved problems in classical physics. Its chaotic and unpredictable nature defies a precise mathematical description, making deterministic approaches largely ineffective. Despite this, all turbulent flows share several characteristic properties. According to Tennekes and Lumley (1972, Chap. 1), turbulent flows are, among other things, highly irregular, diffusive, and dissipative. Another defining feature of turbulence is its multiscale behaviour, wherein turbulent structures of varying length scales coexist within the same flow domain. Turbulent flows are further characterised by large fluctuations in vorticity (Kundu & Cohen, 2012, p. 542), a phenomenon examined in Section 2.3. A universal attribute of turbulent flows is their occurrence at high Reynolds numbers, a dimensionless parameter quantifying the ratio of inertial forces to viscous forces (Schlichting & Gersten, 2016, p. 6–7), defined as

$$\text{Re} = \frac{\mathcal{U}\mathcal{L}}{\nu}. \quad (2.1)$$

In this context, \mathcal{U} represents the characteristic velocity, while \mathcal{L} denotes the characteristic length scale of the flow. The constant ν refers to the kinematic viscosity of the fluid. The Reynolds number is defined based on the specific flow configuration; for instance, for the flow behind a cylinder, the cylinder diameter serves as the characteristic length scale.

Although a closed mathematical framework remains elusive for turbulent fluid flows, fluid motion is fundamentally governed by the Navier-Stokes equations and the continuity equation

$$\frac{\partial u_i}{\partial t} + \frac{\partial(u_i u_j)}{\partial x_j} = -\frac{\partial p}{\partial x_i} + \frac{1}{\text{Re}} \frac{\partial^2 u_i}{\partial x_j \partial x_j} + f_i, \quad (2.2)$$

$$\frac{\partial u_i}{\partial x_i} = 0. \quad (2.3)$$

Here, u_i ($i = 1, 2, 3$) symbolises the instantaneous velocity in the spatial direction i , p corresponds to the pressure, and f_i is used to denote external forces, such as gravitational acceleration. See, for instance, Kundu and Cohen (2012, Chap. 4) for derivations.

Provided that turbulent flows are inherently chaotic and irregular, the instantaneous velocity, u_i , will exhibit temporal fluctuations. For the analysis of turbulent flows, it is therefore helpful to introduce the Reynolds decomposition (Reynolds, 1895), which quantifies these fluctuations, defined as

$$u_i(t) = U_i + u'_i(t), \quad (2.4)$$

where U represents the mean velocity and $u'_i(t)$ denotes the time dependent velocity fluctuations. By applying the Reynolds decomposition into the continuity equation, Eq. (2.3), and substituting the result into Eq. (2.2), the governing equations for turbulent flows can be derived. For details, see, for instance, Pope (2000).

The irregular fluctuations in velocity and pressure provide turbulent flows with a highly diffusive nature. As a result, turbulent flows mix more rapidly than their more organised counterpart, laminar flows. In addition, viscous shear stresses will also lead to dissipation, converting the turbulent kinetic energy

$$k = \frac{1}{2} \overline{u'_i u'_i}, \quad (2.5)$$

into internal energy, leading to an increase in the internal energy of the flow (Tennekes and Lumley, 1972, p. 3).

2.1.1 The energy cascade and the scales of turbulence

Turbulent flows exhibit a wide range of interacting scales, where large-scale motions break down into smaller structures through nonlinear inertial processes. Viscous effects become dominant at the smallest scales, where they dissipate kinetic energy and thus shape the lower end of this multiscale phenomenon. These processes are central to the turbulent energy cascade, in which energy is transferred from large-scale motion to increasingly smaller scales as conceptualised initially by Richardson (1922). These flow structures, commonly referred to as *eddies* or *whirls*, are typically defined as a localised turbulent motion within a specific region of characteristic length scale, L , with a long lifespan compared to other turbulent scales. A more rigorous definition will be provided in Section 2.3. However, this qualitative definition suffices for the present discussion.

Within a turbulent flow, eddies span a wide range of spatial and temporal scales, from the size of the flow domain to the molecular level. These eddies coexist within the same region of the flow (Pope, 2000, p. 183), resulting in turbulence being fundamentally composed of a superposition of motions at multiple scales. Kinetic energy is injected at the largest turbulent scales, and due to the instability

of these large eddies, the energy transfers down to progressively smaller scales. This process continues until the smallest scales, where molecular viscosity becomes dominant and dissipates the kinetic energy into heat (Pope, 2000, p. 182–183).

As mentioned above, turbulent flows are highly irregular (Tennekes and Lumley, 1972, p. 1). However, the velocity fluctuations within such flows are not entirely random. Due to the wide range of interacting eddies at different scales, a distinct pattern emerges when the turbulent flow is decomposed into its frequency components. In contrast to unbiased noise signals, which display a uniform energy distribution across the frequency domain, the kinetic energy in turbulence is distributed in a characteristic, non-uniform manner. An important note is that this applies only when the turbulence is homogeneous and isotropic, that is, when the statistical properties of the flow, such as mean velocity and fluctuation intensity, are uniform throughout the domain and invariant in all directions (Pope, 2000, p. 75–77).

The majority of kinetic energy is contained within the largest eddies (Pope, 2000, p. 187), called the energy-containing range, with eddy-sizes corresponding to the integral length scale L_∞ . This region corresponds to the lowest frequencies in the energy spectrum, while the smallest eddies are associated with higher frequencies and contain less energy. At these small scales, viscous dissipation dominated, and this length scale is referred to as the Kolmogorov scale, η (Kolmogorov, 1941). Between these two extremes lies an intermediate length scale where the energy cascades from large to small eddies without significant viscous effects. This region is known as the inertial subrange (Pope, 2000, p. 187–188).

2.1.2 Turbulent statistics

Even though turbulent flows may differ significantly in turbulence intensity (u'/U), initial conditions and flow geometries, knowledge about their common statistical properties lays the foundation for quantifying different flow parameters. These parameters enable meaningful analysis and comparison across different turbulent flows. However, measuring these swirling structures in the spatial domain is often impractical. When the fluctuations are small compared to the mean flow ($u'_i \ll U_i$), Taylor's frozen-flow hypothesis (Taylor, 1938) offers a practical alternative by allowing time series data at a fixed point to approximate the spatial gradients

$$\frac{\partial u'_1}{\partial x_1} = \frac{1}{U_1} \frac{\partial u'_1}{\partial t}, \quad (2.6)$$

for a mean flow in the x_1 direction. This approximation is based on the assumption that, for small time steps dt , the velocity fluctuations in a turbulent flow are essentially frozen and advected with the mean flow. This approximation forms the theoretical basis for the dimple-tracking method presented in Section 3.3.1.

Assuming isotropic turbulence, the representative turbulent velocity, defined as $\tilde{u}^2 = \frac{1}{3}\overline{u'_i u'_i}$, can be simplified to $\tilde{u}^2 = \overline{u'^2_1}$ (Tennekes and Lumley, 1972, p. 66). Based on this definition, the Taylor microscale (Taylor, 1935), λ_T , is defined as

$$\frac{\overline{\partial u'_1}^2}{\partial x_1} = \frac{\overline{u'^2_1}}{\lambda_T^2}. \quad (2.7)$$

This length scale is related to the inertial subrange and the balance between turbulence production and dissipation. From the Taylor microscale, the Taylor-scale Reynolds number is defined as

$$\text{Re}_\lambda = \frac{\tilde{u}\lambda_T}{\nu}, \quad (2.8)$$

which serves as a measure of the separation of scales in turbulence, in other words, the extent of the inertial subrange (Pope, 2000, p. 242).

Within the energy-containing range, the integral length scale, L_∞ , can be estimated through various approaches. A common and effective way to do this is by defining the normalised autocorrelation function of the velocity fluctuations

$$r_{uu}(\tau) = \frac{\overline{u'(t)u'(t+\tau)}}{\overline{u'^2}}. \quad (2.9)$$

Here, τ describes a time-lag parameter (Pope, 2000, p. 68). Based on this, the integral timescale, T_∞ can be defined as the integral of the normalised autocorrelation function up to the point where it first crosses zero

$$T_\infty = \int_0^{t_0} r_{uu}(\tau) d\tau. \quad (2.10)$$

The zero-crossing time, t_0 , is defined as $r_{uu}(t_0) = 0$. By applying Taylor's frozen flow hypothesis, the integral length scale, L_∞ , can be estimated from the integral time scale as

$$L_\infty = UT_\infty. \quad (2.11)$$

This is the method used in this project. Another approach, used by Aarnes et al. (2025), is to define the integral length scale from the Taylor scale number as

$$L_\infty = \frac{l}{2} \approx \frac{1}{2} \frac{\lambda_T \text{Re}_\lambda}{15}, \quad (2.12)$$

where l is called the macroscale of turbulence (Tennekes and Lumley, 1972, p.273). Further, the turbulent Reynolds number is defined as

$$\text{Re}_\infty = \frac{2\tilde{u}L_\infty}{\nu}. \quad (2.13)$$

One important note is that there are multiple ways to derive and estimate turbulent length scales and parameters. Each of these relies on different assumptions and degrees of approximation. See Fuchs et al. (2022) for an overview and software. The key to these numbers is to enable valid benchmarking and comparison between flows, not to perfectly calculate the exact numerical values, which are often neither feasible to compute nor necessary for most practical applications. Further details regarding the estimation procedures and the resulting parameter values are provided in Sections 3.1.1 and 4.1, respectively.

2.2 Surface dynamics and imprints in free-surface turbulent flows

The interface between two fluids is called a free surface if one of the fluids has a significantly lower viscosity or density than the other. In this case, the shear stress at the surface is zero (Scardovelli and Zaleski, 1999), allowing the surface to move and deform freely. These movements and deformations can result from turbulent motion generated in the bulk flow by the bottom boundary layer, canopies, or submerged jets interacting with the free surface. These surface disturbances are observed, for instance, in river flows, where turbulent motion gives rise to a variety of surface structures. The most significant impact on surface deformation comes from eddies, or turbulent structures, moving along or towards the surface (Brocchini and Peregrine, 2001).

A thorough description of how the turbulence imprints the surface under various conditions is provided by Brocchini and Peregrine (2001). Their framework is initially grounded in turbulent eddies, which they refer to as blobs, characterised by a turbulent length scale, L , and a turbulent velocity scale, q . These scales correspond to the most energetic structures in the flow, and for the analysis later in the report the integral length scale and the root-mean-square velocity, $\sqrt{u_1'^2}$ is used. Although the flow direction and local velocity can vary considerably between individual structures, a single scalar velocity scale, q , is used for simplicity. Using these quantities as coordinate axes, Brocchini and Peregrine (2001) creates an L, q diagram, illustrated by Fig. 2.1, which serves as a foundation for their further discussion of how turbulent motion interact with and influences the free surface.

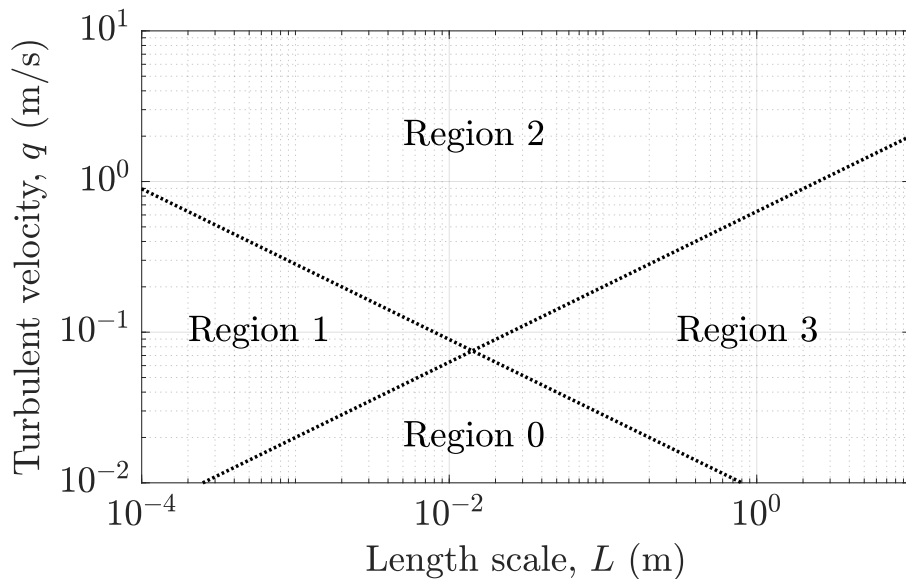


Figure 2.1: The L, q -diagram for water, classifying surface dynamics into four distinct regions. The simplified division of the plane is based on critical Froude and Weber numbers, which define the dividing lines as given in Eq. 2.14. Inspired by Brocchini and Peregrine (2001, Fig. 4).

The regions illustrated in Fig. 2.1 are defined based on the relative influence of gravity and surface tension, which act as stabilising forces at the free surface. Al-

though viscosity also serves as a stabilising force, it is neglected in this framework as turbulent flows occur at higher Reynolds numbers, where the effect of viscosity becomes negligible. To quantify the roles of gravity and surface tension, Brocchini and Peregrine (2001) introduce two dimensionless parameters. The first is the Froude number, defined as $\text{Fr} = q/(2gL)^{1/2}$, which compares the specific turbulent energy $k = \frac{1}{2}q^2$ with the gravitational potential energy, gL . A small Froude number, $\frac{1}{2}q^2 \ll gL$, implies that gravity dominates, resulting in a relatively undisturbed, flat surface. Conversely, at high Froude numbers, $\text{Fr} \gg 1$, turbulent motions are strong enough to overcome gravitational stabilisation, leading to significant surface deformations. The most varied behaviour and interplay between gravity and turbulence is observed for $\text{Fr} \sim \mathcal{O}(1)$ (Brocchini and Peregrine, 2001).

To assess the effect of surface tension, they define the Weber number as $\text{We} = \rho q^2 L / 2\sigma$, where ρ is the fluid density and σ denotes the surface tension. This dimensionless number compares the specific turbulent kinetic energy with the specific surface energy. Aligning with the Froude number, $\text{We} \ll 1$, leads to a nearly undisturbed surface due to the surface tension effects. For $\text{We} \gg 1$, the turbulent energy surpasses the effect of the surface tension, leading to the disintegration of the surface.

Based on critical values of the Froude and Weber numbers, which divide the L, q plane into four regions, each with distinct characteristics. This division is illustrated in Fig. 2.1 where the two dotted lines correspond to

$$q = \sqrt{2\text{Fr}_{\text{crit}}gL} \quad \text{and} \quad q = \sqrt{2\text{We}_{\text{crit}}\sigma/\rho L}. \quad (2.14)$$

Region 0 in Fig. 2.1 is recognised by minimal or no surface disturbances. In this regime, the Froude and Weber numbers are small, indicating weak turbulence. As a result, gravity and surface tension are sufficient to maintain a smooth, undisturbed surface. In Region 1, the Froude number is large, while the Weber number is small. These values imply that surface tension plays an essential role in stabilising the surface, whereas gravity effects are unimportant. The turbulent length scales in this region are typically on the order of $\mathcal{O}(1 \text{ cm})$, and the surface is ‘knobibly’ (Brocchini and Peregrine, 2001). Region 2 corresponds to a flow state where the Froude and Weber numbers are both large, indicating strong turbulence. Neither gravity nor surface tension is strong enough to keep the surface intact, and the flow breaks up into drops and bubbles, resulting in an essentially two-phase flow region. The final regime considered by Brocchini and Peregrine (2001) is the flow conditions commonly observed in rivers and oceans, illustrated in Fig. 1.2. Here, gravity is dominant, and surface tension is relatively weak. The surface is nearly flat, as in Region 1, but the structures appearing are of a much larger length scale.

It is important to note that, due to the broadband nature of turbulence, smaller length scales may carry sufficient energy to induce breakups and surface disintegration, even within stable regions. In practice, real flows rarely correspond to a single point in the L, q diagram (Brocchini and Peregrine, 2001). However, for the experiments analysed in this study, the flow dynamics will generally fall within Region 0 and Region 3.

The orientation and motion of the turbulent structures play a crucial role in how the free surface deforms. Several distinct surface features arise from these interactions and can be linked to the velocity and vorticity beneath the surface.

Three of these, which Brocchini and Peregrine (2001) discuss and are relevant in gravity-dominated free surface flows, are ‘boils’, ‘scars’, and ‘dimples’. Boils are the imprint of a strong upward-moving blob, causing the surface elevation locally to rise (Muraro et al., 2021). At the edge of these upwelling events, the surface elevation dips down, causing the elongated indentations known as scars. A simple illustration of this is presented in Fig. 2.2. Dimples are the imprint of surface-attached vertical vorticity. These structures appear as circular indentations on the surface. Common for these structures, especially scars and dimples, is that they are easily recognisable and hold valuable information about the sub-surface flow field. For example, according to the work of Aarnes et al. (2025), scars are the imprint of horizontally oriented vorticity a certain distance below the surface.

The easily recognisable nature of these structures and their link to sub-surface flow make them very interesting in terms of non-contact measurement applications. As discussed in Chapter 1, measurements of these structures at the surface could have the application of estimating the gas transfer rate between air and water at a cheaper cost than *in situ* measurements (Dolcetti et al., 2022). For example, as mentioned above, Babiker et al., 2023 suggest that dimples can serve as a proxy for surface divergence. Their distinct visual appearance makes them easy to identify, and their strong association with upwelling processes is particularly relevant, given the critical role of surface renewal in gas transfer dynamics (Kermani and Shen, 2009).

Several studies, for instance, McKenna and McGillis (2004), show the close correlation between gas transfer rates and surface divergence in free-surface turbulence. A large positive surface divergence is related to the event of upwelling boils, which renew the surface with fluid not in equilibrium with the atmosphere, enabling heat transfer (Veron et al., 2011). Common for most studies investigating this relation is that they have used the surface divergence. For this specific project, due to the lack of surface velocity fields, the horizontal divergence in the sub-surface plane will be investigated. Although a standard notation for surface divergence uses β , this thesis employs another notation to avoid confusion. Horizontal divergence describes how much a fluid spreads or converges in the plane. A positive value is related to spreading, and vice versa for a negative value. Calculated from surface-normal velocity gradients, the mean square horizontal divergence is defined as

$$\overline{D_h(t)^2} = \overline{\left(\frac{\partial u_1}{\partial x_1} + \frac{\partial u_2}{\partial x_2} \right)^2}, \quad (2.15)$$

where the overline describes the spatial average over the plane. The analysis and discussion regarding horizontal divergence and its correlation with dimple counts are provided in Section 4.5.

2.3 Fundamentals of vorticity and vortex dynamics

This section introduces the concept of vorticity, along with a discussion of its production, transport, and diffusion. As briefly noted in Section 2.1, turbulent flows are characterised by, among other features, high levels of fluctuating vorticity

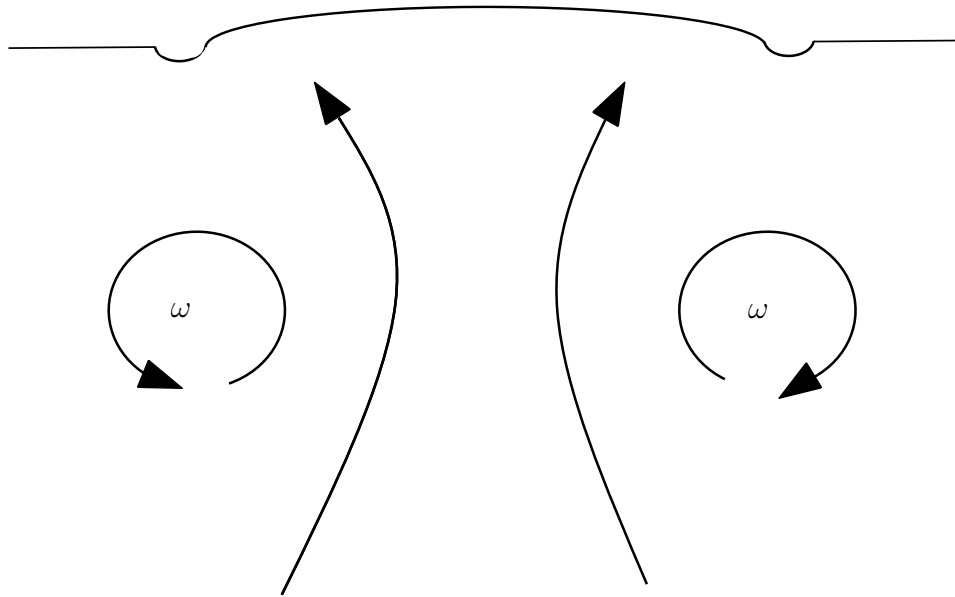


Figure 2.2: Cross-section of a simplified upwelling event illustrating the formation of scars. A vortex loop, depicted as two counter-rotating vortices, transports fluid upward toward the free surface, creating a localised elevation rise known as a boil. At the edges of the boil, the surface depresses, forming the elongated scars.

(Kundu and Cohen, 2012, p. 542). Vorticity describes the local rotational motion within a fluid and is mathematically defined as the curl of the velocity field

$$\omega_k = \epsilon_{ijk} \frac{\partial u_j}{\partial x_i}, \quad (2.16)$$

where ϵ_{ijk} is the Levi-Civita tensor accounting for the antisymmetric nature of the curl operation. When fluid elements move along nearly circular streamlines, the motion is referred to as vortex motion, and the curve that is tangent to the local vorticity vector is called a vortex line (Kundu and Cohen, 2012, p. 172). Multiple vortex lines passing through a tubular surface is called a vortex tube, and these tubes have one very important characteristic. The strength of a vortex tube, defined as the circulation on a closed circuit on the surface of the tube, is constant along its length. This conservation implies that said tubes cannot end suddenly within the fluid; they have to form a loop or terminate on solid or free surfaces (Kundu and Cohen, 2012, p. 179). Relating this to the vague definition of eddies, or blobs, in Section 2.1, an eddy may be interpreted as a region of concentrated vorticity within the flow.

As discussed, vortex tubes have a constant strength along their length, and they cannot terminate within the fluid. These are two of Helmholtz's vortex theorems (Kundu and Cohen, 2012, p. 179), which describe how vorticity evolves in a flow. The two other theorems say that vortex lines move with the fluid and that the strength of a vortex tube remains constant in time. The former implies that vortices will move along with the mean flow, a matter related to Taylor's frozen flow hypothesis, introduced in Section 2.1.2, and a key assumption in developing the computer vision method in Section 3.3.1. The last theorem is a consequence of Kelvin's persistence of circulation theorem, which states that in an inviscid, barotropic flow acted upon by conservative body forces, the circulation around a

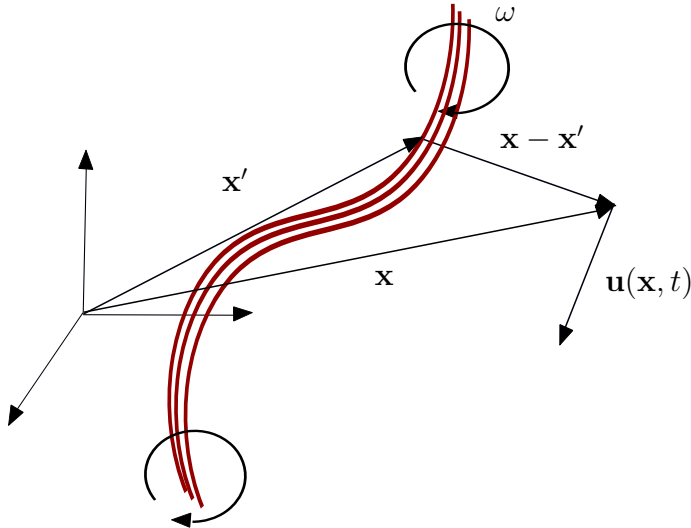


Figure 2.3: Conceptual illustration of velocity induction by a vortex tube. The red curves illustrate vortex lines collectively forming a vortex tube, with the volume V' encapsulating a segment of this structure. This visualisation is inspired by Kundu and Cohen (2012, Fig. 5.8).

closed curve moving with the flow remains constant in time (Kundu and Cohen, 2012, p. 176). This connection describes why the turbulent eddies are long-lived compared to other turbulent timescales. However, real flows are not inviscid. Viscous effects will cause diffusion of vorticity and change the circulation. The time evolution of vorticity is described by the vorticity equation, which is found by taking the curl of Eq. (2.2), such that

$$\epsilon_{kli} \frac{\partial}{\partial x_l} \left[\frac{\partial u_i}{\partial t} + \frac{\partial(u_i u_j)}{\partial x_j} \right] = -\frac{\partial p}{\partial x_i} + \frac{1}{\text{Re}} \frac{\partial^2 u_i}{\partial x_j \partial x_j} + f_i. \quad (2.17)$$

Using Eq. (2.16) and the antisymmetric relations, one obtains

$$\underbrace{\frac{\partial \omega_i}{\partial t}}_{\text{Temporal change}} + \underbrace{u_j \frac{\partial u_i}{\partial x_j}}_{\text{Advection term}} = \underbrace{\omega_j \frac{\partial u_i}{\partial x_j}}_{\text{Vortex stretching}} + \underbrace{\nu \frac{\partial^2 \omega_i}{\partial x_j \partial x_j}}_{\text{Viscous diffusion}}. \quad (2.18)$$

The first term on the right-hand side of Eq. (2.18) describes how vorticity is changed due to the stretching and tilting of vortices. The last term is the nonzero term that describes how viscosity changes the vorticity.

In a turbulent flow, numerous vortex tubes interact with each other and the local velocity field. Analogous to how electric currents induce a magnetic field around them, vortex motion induces velocity in the surrounding fluid. Both these phenomena can be described using the same mathematical framework. The law of Biot and Savart describes how the magnetic field around a steady current (Griffiths, 2013). Similarly, in fluid mechanics, by taking the curl of the vorticity, the velocity induced by vorticity is obtained as

$$\mathbf{u}(\mathbf{x}, t) = \frac{1}{4\pi} \int_{V'} \frac{\boldsymbol{\omega}(\mathbf{x}', t) \times (\mathbf{x} - \mathbf{x}')}{|\mathbf{x} - \mathbf{x}'|^3} d^3 \mathbf{x}', \quad (2.19)$$

and illustrated in Fig. 2.3. In this formulation, V' describes a segment of the vortex. The vorticity is concentrated in the source point \mathbf{x}' , while the velocity is induced at the observation point \mathbf{x} . The complete derivation is provided in standard fluid mechanics textbooks, for example, Kundu and Cohen (2012, p. 181–183).

2.4 The surface layer in free-surface turbulent flows

Observing the free surface from above, the imprints discussed in Section 2.2 are visible. These imprints are the result of turbulence interacting with the surface and the boundary conditions that the surface imposes on the flow. For gravity-dominated flows, where the Froude number is small, the deviations from the undisturbed surface, $x_3 = 0$, are minimal. Due to the assumption that the fluid on the opposite side of the free surface has a negligible viscosity, the tangential stresses are zero at the surface where $x_3 = 0$ (Shen et al., 1999)

$$\frac{1}{\text{Re}} \left(\frac{\partial u_1}{\partial x_3} + \frac{\partial u_3}{\partial x_1} \right) = 0, \quad (2.20)$$

$$\frac{1}{\text{Re}} \left(\frac{\partial u_2}{\partial x_3} + \frac{\partial u_3}{\partial x_2} \right) = 0. \quad (2.21)$$

While dimples are the imprints of vertically oriented vorticity, the elongated scars, introduced in Section 2.2, are the imprints of horizontal vorticity. However, as Aarnes et al. (2025) confirms numerically, the concentration of horizontal vorticity is located a distance below the scar, not attached to the surface as dimples. This result can be explained mathematically using the fact that u_3 is small at the surface for small values of Fr and the constraint of Eq. (2.21). Following this, vorticity in the x_1 direction at the free surface is defined as

$$\omega_1 = \frac{\partial u_3}{\partial x_2} - \frac{\partial u_2}{\partial x_3} = 2 \frac{\partial u_3}{\partial x_2} \approx 0 \quad \text{at } x_3 = 0. \quad (2.22)$$

The same argument holds for vorticity in the x_2 direction, showing that horizontally oriented vorticity is absent at the free surface. Another important relation for the vorticity at the surface is shown by Shen et al. (1999) who after taking the divergence of Eq. (2.16) obtain

$$\frac{\partial \omega_k}{\partial x_k} = \frac{\partial}{\partial x_k} \left(\epsilon_{ijk} \frac{\partial u_j}{\partial x_i} \right). \quad (2.23)$$

The right side of Eq. (2.23) equals zero, indicating that the vorticity field is divergence-free. This condition, along with (2.22) leads to

$$\frac{\partial \omega_3}{\partial x_3} = 0 \quad \text{at } x_3 = 0, \quad (2.24)$$

which implies that the vertical component of the vorticity does not vary significantly with depth near the free surface. These results shows that there exists a surface layer where the values of ω_1 , ω_2 and $\partial \omega_3 / \partial x_3$ change from their outer values to their smaller values close to the free surface (Shen et al., 1999). This region, referred to as the *viscous layer*, is thin for high Reynolds numbers, and the

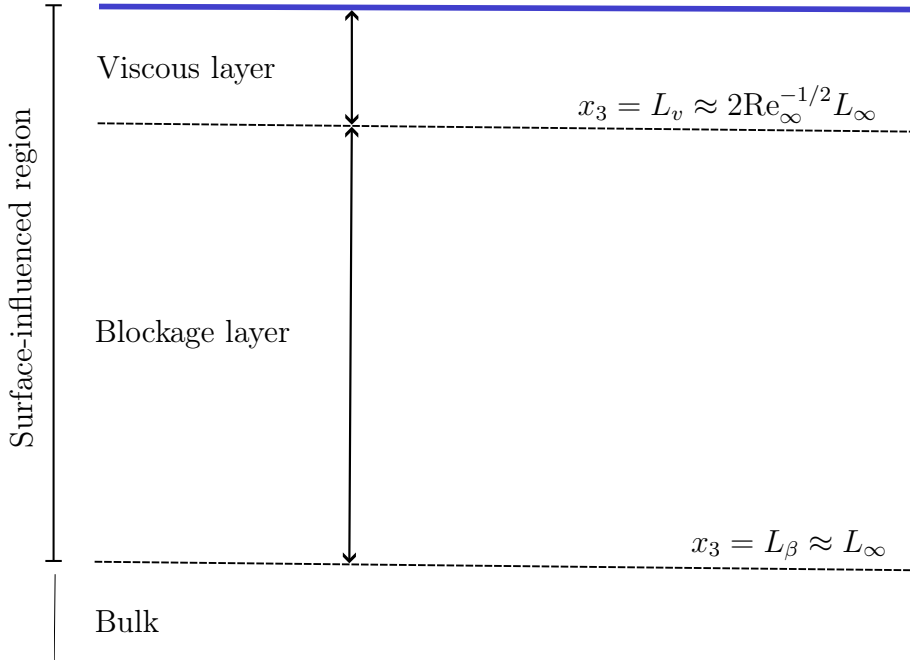


Figure 2.4: Schematic of the surface layer in turbulent free-surface flows. The blue line represents the surface, with the surface-influenced region consisting of the thin viscous layer and the slightly larger blockage layer. The bulk of the flow is located outside the surface-influenced region. Note that the schematic is not to scale.

thickness of this layer scales as $L_v \sim Re_\infty^{-1/2}$. Based on measurements by Brumley and Jirka (1987) and the discussion by Magnaudet (2003), the viscous-layer thickness is estimated as $L_v = 2Re_\infty^{-1/2} L_\infty$.

In addition to the thin viscous layer, there exists a thicker layer, called the *blockage layer*, with a thickness $L_\beta \sim \mathcal{O}(l)$, where l is the macroscale of the turbulence. A schematic of the near-surface region is presented in Fig. 2.4. Within the blockage layer, the turbulence intensity is redistributed, meaning the vertical velocity fluctuations decrease and the horizontal velocity fluctuations increase (Shen et al., 1999). The thickness of this region is of the order of the integral length scale, and it is both conventional and practical to set $L_\beta = L_\infty$, consistent with the approach used by several others (Magnaudet, 2003; Guo and Shen, 2010; Herlina and Wissink, 2014; Aarnes et al., 2025). Outside these surface-affected layers lies the bulk flow, where turbulence is no longer significantly influenced by the presence of the free surface.

Dimples are observed to be highly persistent once attached to the surface. By analysing the vorticity equation, Eq. (2.18), in the direction normal to the surface, Shen et al. (1999) find, when defining

$$\alpha = \tan^{-1}((\omega_1^2 + \omega_2^2)^{1/2} / |\omega_3|), \quad (2.25)$$

to be the inclination angle of the vorticity at $x_3 = 0$, that both vertical vortex stretching and dissipation decrease significantly for smaller α . This means that nearly vertical vortices, associated with dimples, experience less decay and are therefore more persistent once attached. More details on results and derivations of surface-attached vorticity are found in Shen et al. (1999, Ch. 4).

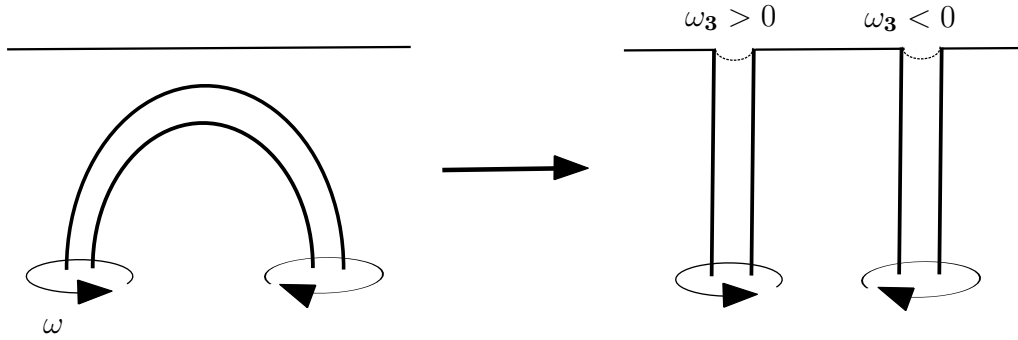


Figure 2.5: Simplified illustration showing how the head of a vortex loop, swept toward the surface during an upwelling event, breaks apart and attaches two counter-rotating vortices to the surface. The horizontal vorticity in the head region is dissipated within the surface layer, as described in Section 2.4.

Relating this to the theorems of Helmholtz, introduced in Section 2.3, which says that vortex tubes cannot end within the fluid but must create loops or terminate at the free surface. These loops exist in the bulk of the flow and can rise toward the surface in upwelling events; see Fig. 1.2. However, as the loop approaches the surface, the horizontal vorticity dissipates more rapidly than the vertical vorticity in the surface layer, causing the loop to break up and form two counter-rotating vortices that attach to the surface. This process is illustrated in Fig. 2.5. Therefore, dimples come in pairs, where one has positive vorticity and the other has negative vorticity, and once they are attached to the surface, they tend to persist.

2.5 The optics of surface reflections

When light strikes a flat surface, the light rays are reflected at an angle equal to the angle of incidence, while some of the incident light refracts into the medium. However, when the surface is disturbed, the reflections are influenced by the local curvature of the surface. As illustrated in Fig. 2.6, disturbances on the surface will alter the reflection angles of incoming light. These variations in reflection angles create distinctive patterns, effectively encoding information about the surface gradients. Thus, analysis of these reflected patterns enables indirect measurement of the surface elevation. The concave regions corresponding to indentations of the surface cause light rays to concentrate and reflect a brighter region on the projector screen. Conversely, a darker area on the projector screen is caused by a convex region, where light has spread out. The brighter areas can, therefore, be linked directly to the indentations caused by dimples and scars, described in Section 2.2.

In the experiments conducted within this project, described in Section 3.1, rhodamine was added to the water in the channel to alter its refractive properties, thereby increasing surface reflectivity. Under the assumption of near-total reflection of incident light, and given that surface gradients remain relatively small despite turbulence-induced surface variations, the reflected image of the surface is hypothesised to serve as a robust proxy measure of the free-surface topography without direct measurement of the surface itself.

Recent studies have shown that the scattering of light from a rough surface pro-

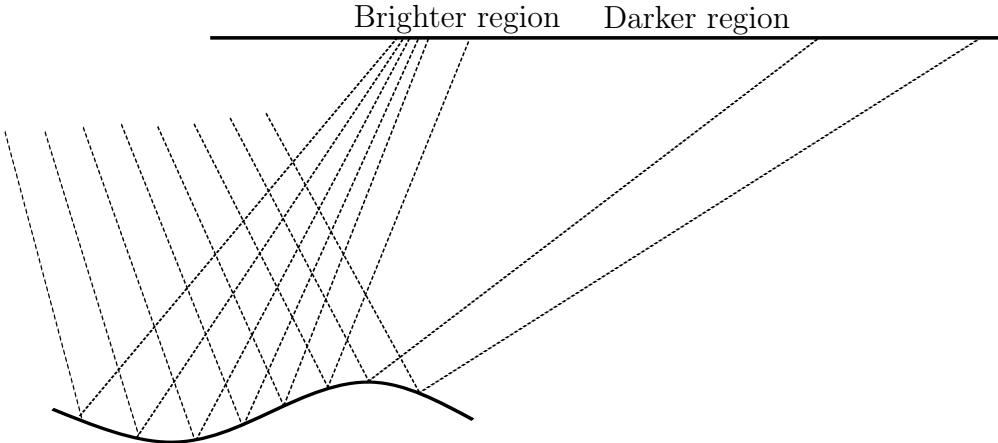


Figure 2.6: Illustration of light ray reflection from a disturbed surface. Concave regions (left) focus reflected light, creating brighter areas on the projector screen, whereas convex regions (right) spread reflected light, leading to darker areas.

duces visually observable brightness variations and encodes quantitative statistical information about surface topography. In particular, Simonsen et al. (2021) developed a nonparametric inversion approach, based on the Kirchhoff approximation and stationary-phase methods, to reconstruct key statistical properties, such as surface root mean square roughness and height-height correlation function, from in-plane, co-polarised light scattering data. Although their work involves advanced mathematical techniques and exceeds the scope of this project, it demonstrates that the patterns observed in surface reflections can be linked to the underlying surface profile. A different, but somewhat related, work by Dolcetti et al. (2021) uses microphone arrays and sound scattering to reconstruct the rough surface elevation profiles. These works suggest that it may be possible to obtain the full surface elevation profile from optical reflections alone, which could possibly pave the way for more innovative remote sensing applications.

Chapter 3

Methods

Where Chapter 2 outlined the theoretical framework for turbulent motion interacting with a free surface, this chapter focuses on the methods used to analyse such flows, specifically for this project. The chapter begins by describing the experimental setup used to collect the flow data in Section 3.1, followed by an introduction to wavelet analysis in Section 3.2, which serves as the foundation for the wavelet-based computer vision method developed in this work for detecting and tracking dimples. This method is described in Section 3.3. Furthermore, the methodology for vortex detection within velocity fields is presented in Section 3.4, along with the performance metrics used to evaluate the detection and tracking results in Section 3.5.

3.1 Experimental setup

The data analysed in this project were acquired in the recirculating open water channel at the Norwegian University of Science and Technology (NTNU, Trondheim), a facility that Jooss et al. (2021) describes thoroughly. In the experimental campaign conducted by another team within the research group, simultaneous measurements were carried out using Fourier transform profilometry (FTP) to capture the surface topology and Stereoscopic particle image velocimetry (SPIV) to measure the velocity field at a depth of $d = 10$ mm below the surface. Additionally, the light reflected from the surface onto the ceiling was recorded using a GoPro HERO 12 camera.

Figure 3.1 shows a simplified schematic of the experimental setup and the three measurement planes. A thorough description of the full experimental setup is beyond the scope of this project and will be provided in a forthcoming publication. Here, only a brief overview of the methodology behind SPIV and FTP is provided. Particle image velocimetry (PIV) is an optical flow measurement technique where a pulsed laser sheet illuminates tracer particles seeded into the flow. By cross-correlating their displacements between successive images, the instantaneous velocity field can be estimated. SPIV builds on the same principles but uses two cameras to resolve all three velocity components. See Prasad (2000) for more details. Fourier transform profilometry is a non-contact optical measurement technique in which a fringe pattern is projected onto the surface and processed via Fourier transforms to obtain the surface elevation profile. A review is provided by X. Su and Chen (2001).

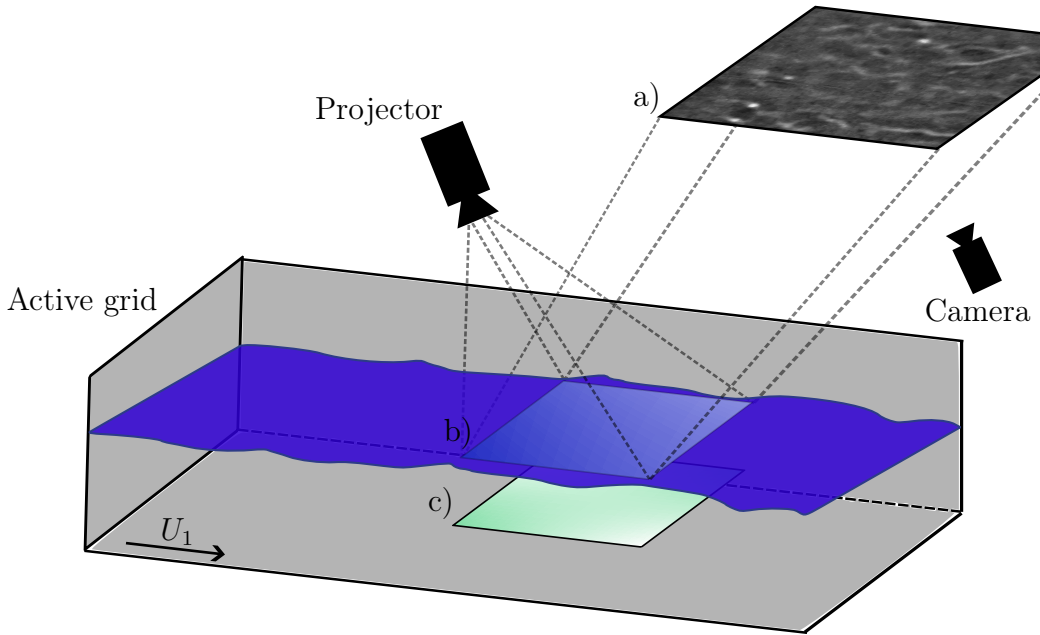


Figure 3.1: Schematic of the experimental setup used for data acquisition in this project. In the open-water channel (NTNU, Trondheim), turbulence is generated using an active grid, and three simultaneous measurements are conducted. **a)** Surface reflections produced by the projector onto the projector screen in the ceiling are recorded from below with a camera. In this figure, the reflected pattern is placed above for illustrative purposes. **b)** The surface, illuminated by a projector, corresponds to the measurement plane of the Fourier transform profilometry. **c)** Field of view for the SPIV measurements at a depth $d = 10$ mm.

For the experiment analysed in this project, the flow enters the water channel with a mean velocity of $U_1 \approx 0.25$ m/s, and turbulence is generated upstream of the measurement region using an active grid with a mesh size of $M = 10$ cm and the grid bar rotating at 1 Hz. See Jooss et al. (2021, App. B) for more details. The turbulent parameters specific to this flow will be presented and discussed in Section 4.1.

For the SPIV measurements, the field of view covered a horizontal plane spanning $30\text{ cm} \times 30\text{ cm}$, recorded at a depth $d = 10$ mm, with an acquisition rate of 15 Hz. The measurement location was $60M$ downstream of the active grid. At the surface, the processed profilometry captured a field of view of $36.5\text{ cm} \times 28.8\text{ cm}$ at an acquisition rate of 45 Hz synchronised with the SPIV measurements. The surface reflection recordings had an initial frame rate of 59.94 Hz and a resolution of 3840×2160 pixels. However, the video was post-processed, calibrated, and downsampled before analysis, as outlined in Section 3.1.2.

3.1.1 Laser Doppler velocimetry

To estimate the turbulent statistics of the flow, as outlined in Section 2.1.2, Laser Doppler Velocimetry (LDV) was used. LDV is a non-intrusive technique that provides pointwise flow velocity measurements by detecting the Doppler shift of scattered laser light from seeding particles. The technique yields a high-resolution time series of velocity in the free stream. This thesis will not provide a comprehen-

hensive treatment of the theory behind LDV. For further details, see, for instance, Foreman et al. (1965) and Yeh and Cummins (1964).

One of the key challenges in using LDV for calculating turbulent statistics is that velocity measurements are event-based, occurring as particles pass through the measurement volume, resulting in a non-uniformly sampled time series. To enable the calculation of time derivatives, the data must be resampled onto a uniform time grid. For this purpose, sample-and-hold interpolation is applied, following the method proposed by Nobach et al. (1998), where each measured velocity is assumed constant until the arrival of the next particle. The resulting time series is reconstructed at the average sampling frequency.

For estimating the turbulent parameters, two LDV measurements are used: one near the surface at a depth $d = 20$ mm and another located deeper within the bulk region of the flow. These measurements were obtained 50 cm upstream of the SPIV field of view.

3.1.2 Post-processing and calibration of reflection video

Due to the simultaneous acquisition of the three datasets in the experimental procedure, the surface reflection video required substantial post-processing. The green laser light from the other measurements contaminated some of the video frames, making them unusable. Additionally, to enable meaningful analysis, the surface coordinates had to be mapped onto the reflection video.

To address the green laser light contamination, all frames with a green channel intensity exceeding 25 were removed. This filtering resulted in the complete loss of certain segments of the time series, while the retained parts had every other frame discarded on average. After the green light filtering, the video was converted to grayscale. Further, two methods were applied to correct for camera distortion. First, MATLAB's Camera Calibrator app was used to correct lens distortion by capturing a series of checkerboard images at varying orientations and distances. This method automatically detects corner points and calculates the intrinsic parameters of the camera, as well as the distortion parameters. The resulting radial distortion was low ($k_1 = -0.0065$, $k_2 = 0.0055$), and it was used to undistort the full video, enabling the analysis of geometrically corrected data.

Second, because the projector illuminated the surface at an angle, the reflections in the ceiling were geometrically distorted. The method for correcting this involved placing a rectangular, dotted-pattern plate on the surface and capturing its reflections on the projector screen. By manually identifying four corner points of this reflected pattern, a projective mapping could be computed, warping the image back into an accurate rectangle. This correction paved the way for a precise alignment with the surface coordinate system.

To accurately align the coordinate system of the surface with the surface reflection video, a feature-based alignment method was employed using sub-surface flow field data. More specifically, by aligning the strongest vortical structures in the sub-surface λ_2 field and manually matching these with surface dimples, a coordinate transform was created. The principles of λ_2 are introduced in Section 3.4. This calibration was performed on the first approximately 20 seconds of 240 seconds of available data. While the profilometry data was also considered for this purpose, it proved too noisy for precise alignment. Autocorrelation-based

methods could also have provided a more robust transform. These considerations are revisited in Chapter 4 and in Section 4.6, where limitations and potential improvements to the calibration strategy are further discussed.

3.2 Wavelet analysis

As with turbulent signals, many natural signals are composed of a range of different frequencies. A common feature of such signals is that low-frequency components tend to persist for longer periods, while high-frequency parts have a shorter lifespan. Fourier analysis is an effective method for decomposing a signal into its constituent frequencies. However, if these signals are nonstationary, Fourier analysis meets its major limitation, as it contains no information about when or where specific frequencies occur (Antoine et al., 2004, p. 1). To overcome this, the Wavelet Transform can be used to decompose a signal into both time (or spatial) and frequency components using a multi-resolution approach. The Wavelet transform is obtained by first defining a so-called mother wavelet ψ , which can be stretched and translated, defined as

$$\psi_{s,b} = \frac{1}{\sqrt{s}}\psi\left(\frac{t-b}{s}\right). \quad (3.1)$$

Here, the constant s will dilate or contract the basis function, ψ , without altering the shape. The constant, b , will translate the function in time (Antoine et al., 2004, p. 4). Further, the wavelet decomposition of a signal $f(t)$ is found by taking the convolution between the signal and ψ , such that

$$W(f)(s, b) = \langle f, \psi_{s,b} \rangle = \int_{-\infty}^{\infty} f(t)\psi_{s,b}^* dt. \quad (3.2)$$

Regarding the limitations of Fourier analysis, which fail to accurately estimate the temporal variation of a time-dependent signal, similar limitations also apply to Wavelet analysis. There exists a fundamental uncertainty principle for time-frequency analysis, setting a limit on the resolution that can be obtained simultaneously in both the time and frequency domains (Brunton and Kutz, 2019, p. 80–81). This uncertainty principle, thoroughly described by, for instance, Mallat (1999, p. 30–33), states that the product of the variances of time and frequency must exceed a certain constant. This forms the mathematical reasoning behind Heisenberg’s uncertainty principle in quantum mechanics (Heisenberg, 1927).

In wavelet analysis, the limitations imposed by the uncertainty principle are partially avoided by the stretching and squeezing of the mother wavelet. The wavelet can be compressed to match high-frequency components, enhancing temporal resolution while reducing frequency resolution. To capture the low-frequency components, the wavelet can be stretched, which improves the frequency resolution at the cost of temporal precision. This also reflects the practical needs of signal analysis and the nature of high- and low-frequency components. For high-frequency events, it is often more important to know when they occur rather than to distinguish them accurately by frequency, as they usually are more short-lived. On the other hand, for low-frequency components, precise timing is less critical, but accurate frequency resolution is more essential.

3.2.1 Two-dimensional wavelet analysis

The extension of wavelet analysis to two dimensions follows naturally from the one-dimensional case. However, in two dimensions, simple dilating and translating of the basis function are insufficient to capture the full range of structural features. Specifically, two-dimensional data often contains directional features that require sensitivity to orientation. To capture this, the mother wavelet must also be rotated (Antoine et al., 2004, p. 32–36). Therefore, in addition to dilation by a factor s and translation by a vector $b \in \mathbb{R}^2$, the wavelet is now rotated using a rotation matrix

$$r_\theta = \begin{bmatrix} \cos \theta & -\sin \theta \\ \sin \theta & \cos \theta \end{bmatrix}. \quad (3.3)$$

Including the rotational operation into Eq. (3.1), the following basis function for two-dimensional wavelet analysis is obtained

$$\psi_{s,\mathbf{b},\theta} = \psi \left[r_\theta^{-1} \left(\frac{\mathbf{x} - \mathbf{b}}{s} \right) \right]. \quad (3.4)$$

This leads to the two-dimensional wavelet transform of the signal, $f(\mathbf{x})$, which becomes

$$W(f)(s, \mathbf{b}, \theta) = \langle f, \psi_{s,\mathbf{b},\theta} \rangle = \int_{\mathbb{R}^2} f(\mathbf{x}) \psi_{s,\mathbf{b},\theta}^* d\mathbf{x}. \quad (3.5)$$

However, the rotational term will not contribute if an axisymmetric wavelet is used, which will be the case for this project and discussed in Section 3.3.

A valuable application of the two-dimensional wavelet transform is to analyse images and utilise the ability to decompose both frequency and spatial information for object detection. The method enables effective detection of edges and shapes at various scales and orientations (Grossmann, 1988), features that are fundamental in identifying objects, utilised in Section 3.3. Due to the relatively uniform size of the dimples, the method presented in the next section will not utilise the multi-resolution capabilities of wavelet analysis. However, wavelets remain a powerful tool for detecting structures of varying scales in images, making them well-suited for computer vision tasks where features of interest appear at different scales.

3.3 Computer vision technique

The computer vision method used in this project is based on the works of Babiker et al. (2023) and Aarnes et al. (2025), who used two-dimensional wavelet transforms to detect and track the surface features of interest, as this method is highly efficient in emphasising edges (Grossmann, 1988). In these works, they, unlike this project, used the wavelet transform directly on the surface elevation. The hypothesis is that the same method will work as efficiently for the surface reflections as the convex parts of the flow will concentrate the light and create brighter spots, and vice versa for the convex structures, as introduced in Section 2.5. As a note, however, to facilitate comparison between the different data in Section 4.4, the wavelet transform will also be applied directly to the surface elevation profile obtained from the profilometry.

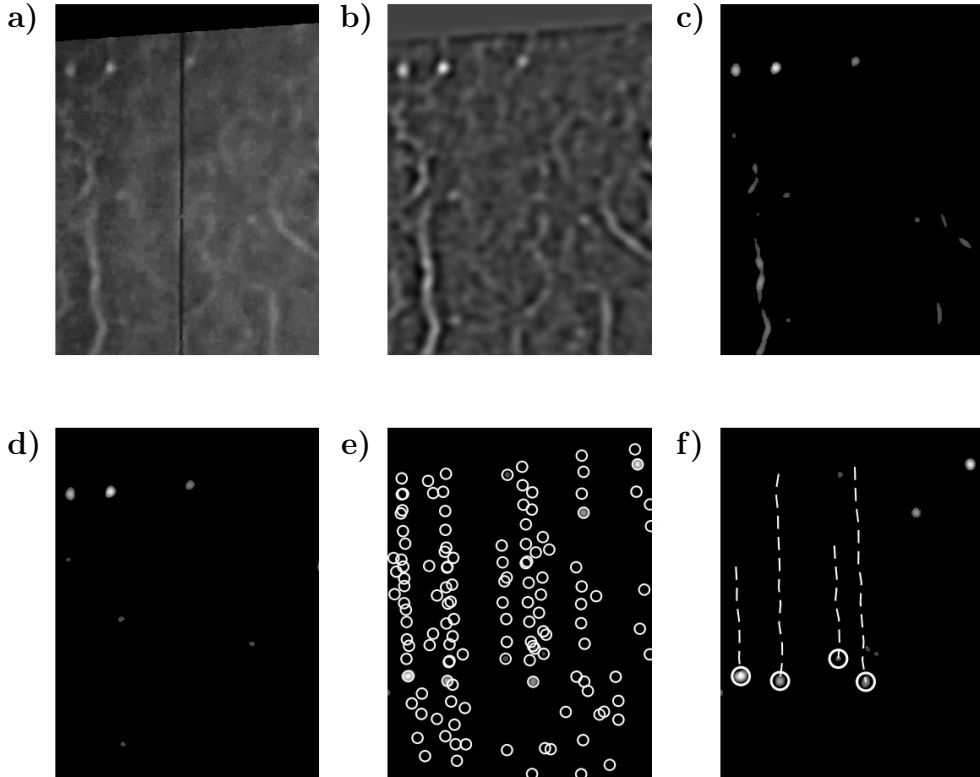


Figure 3.2: Visualisation of the wavelet-based computer vision and dimple tracking method. **a)** Original grayscale video; **b)** Wavelet transform $W(x_1, x_2)$ of the ceiling video; **c)** Connected regions where $W > W_{\text{thr}}$; **d)** Connected regions filtered for eccentricity < 0.85 and solidity > 0.6 ; **e)** All detected dimples over a period of $\sim 1T_\infty$ without tracking; **f)** Structures tracked and filtered for lifetime with $t_{\min}/T_\infty = 0.105$.

The whole dimple detection process is described in Fig. 3.2 and is initialised by importing a snapshot of the post-processed surface reflection video. Further, the two-dimensional continuous wavelet transform, introduced in Section 3.2, of this snapshot, is computed for a scale, s . For this project, the Mexican hat wavelet, also known as the Marr wavelet, is used. This wavelet is defined in the MATLAB function *cwtft2* in the Wavelet Toolbox (MathWorks, 2024) in the Fourier domain. By taking the inverse Fourier transform, this wavelet is defined as

$$\psi(x_1, x_2) = (2 - x_1^2 + x_2^2)e^{-(x_1^2+x_2^2)/2}, \quad (3.6)$$

in the spatial domain. Due to its axisymmetric nature, this wavelet performs well at highlighting circular patterns. This aligns with the observations of Babiker et al. (2023) and also implies that the orientation of the wavelet is unimportant, as discussed in Section 3.2.1.

By keeping the wavelet coefficients, $W > W_{\text{thr}}$, only the brightest parts of the video are retained, corresponding to scars, dimples and some artefacts of the surface ripples. This filtering is illustrated in Fig. 3.2 (c). The appropriate values of s and W_{thr} are determined through practical considerations and will be discussed thoroughly in Section 4.2.1. Given that dimples leave a circular indentation on

the surface (Brocchini and Peregrine, 2001), the connected structures and wavelet coefficient filtering are further refined using the shape descriptors *eccentricity* and *solidity* to obtain only the most circular features, visualised in Fig. 3.2 (d). These measures quantify and categorise the detected structures, excluding non-circular shapes based on the appropriate choice of thresholds. Eccentricity, \mathcal{E} , describes the deviation from a perfect circle. A straight line will have an eccentricity of $\mathcal{E} = 1$, while a perfect circle will have $\mathcal{E} = 0$. By applying an eccentricity threshold, elongated or irregular features are discarded, usually corresponding to scars. The shape filtering ensures that only nearly circular structures, consistent with the typical appearance of a dimple, are considered. However, scars that bend into a circular shape will be falsely identified as dimples if the filtering is based solely on eccentricity. Filtering for solidity will mitigate this problem, as this measures the compactness of a structure. It measures the ratio between the structure and the smallest convex shape encapsulating it. By requiring the dimple candidates to have a high solidity, bent scars will be filtered out. The choice of the threshold values of the shape descriptors will be discussed in Section 4.2.1.

3.3.1 Dimple tracking

Working with experimental data introduces noise and imperfections to the data compared to direct numerical simulations. For this project, this problem arises after the circular structures are identified using wavelet analysis. Surface ripples could, like dimples, create circular indentations to the surface and in the surface reflections, and with the method presented in Section 3.3, there are few ways of determining whether the circular structure is noise or a real dimple. The approach used in this project leverages two fundamental characteristics of dimples: first, they persist for a long time, and second, they advect with the mean flow, as discussed in Section 2.2 and Section 2.3, respectively. It is noted here that Savelsberg et al. (2006) finds that although Taylor's frozen flow hypothesis works well for sub-surface vortices, it does not do so for the free surface due to gravity-capillary waves. Nevertheless, the method for dimple tracking used in this project performs sufficiently at the free surface if a proper error radius is imposed.

Compared to the method of Babiker et al. (2023) for tracking dimples in direct numerical simulations, their approach defined a dimple as the same structure if the detected region overlapped with the detected region in the previous timestep. However, as the present study utilises experimental data with a significantly lower time resolution and a mean flow, an alternative method is developed.

The concept of the dimple tracking method is illustrated in Fig. 3.3 and begins with an initial identification of a circular candidate dimple at timestep t , called ∇_i . Assuming the dimple advects with the mean flow, the search for this structure in the next timestep, $t + dt$, begins a distance, $\Delta = U_1 dt$, downstream of the position of the dimple in timestep t . Here, Δ represents the displacement of the mean flow during one timestep. However, as introduced in Section 2.4, vorticity elsewhere in the flow can induce a local velocity on the dimple of interest and alter its trajectory slightly. Therefore, an error radius, r_e , around the expected location of the dimple in timestep $t + dt$ is introduced to account for these perturbations.

The dimple tracking method proposed is designed to account for non-uniform time resolution, as this was the case in the surface reflection data after green light

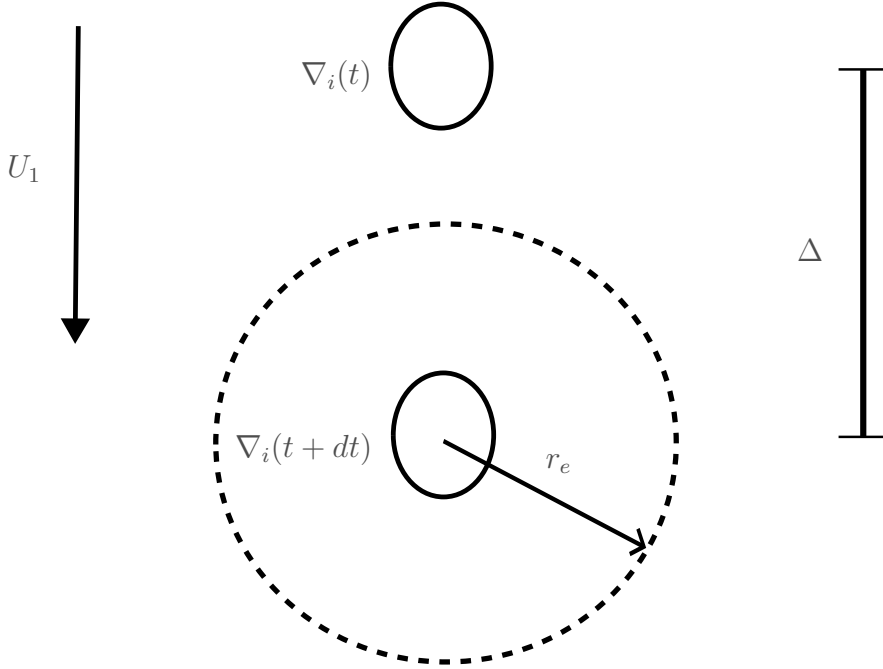


Figure 3.3: Illustration of the dimple tracking method. A dimple, ∇_i , detected at time t , is expected to advect a distance $\Delta = U_1 dt$ downstream by the mean flow in the subsequent timestep. However, the trajectory may deviate from a linear path due to induced velocity from surrounding vorticity. To account for this, the method searches for the dimple within a radius r_e around the predicted downstream position.

filtering, as discussed in Section 3.1.2. If the time series is non-uniform and the next timestep is $t + ndt$, the new search location will be $n\Delta$ downstream of the initial observation. If there are gaps in the time series larger than 5 time steps, corresponding to approximately $0.35T_\infty$ for the reflection video, the tracking stops automatically.

An example of the dimple tracking method on the surface reflections is shown in Fig. 3.2, where all potential dimples are identified over a few time steps in Fig. 3.2 (e) and filtered for a minimum lifetime $t_{\min} = 0.105T_\infty$ in Fig. 3.2 (f).

3.4 Vortex core detection in the sub-surface flow region

In the sub-surface region, a method is required to separate vortices from the rest of the flow. This will enable the possibility to quantify the relationship between surface detections and the underlying flow structures, discussed in Section 4.3. For this purpose, the λ_2 criterion proposed by Jeong and Hussain (1995) is used. This measure distinguishes between shearing and swirling motion in a flow. Based on the velocity gradient tensor, $\partial_j u_i$, it involves its decomposition into the strain-rate tensor \mathbf{S} and the rotation-rate tensor $\boldsymbol{\Omega}$. The quantity λ_2 is the median eigenvalue of the matrix $\mathbf{S}^2 + \boldsymbol{\Omega}^2$. Negative regions of the λ_2 field indicate that swirling motion dominates, corresponding to the presence of vortex structures.

A local minimum in the λ_2 field is associated with a region of lower pressure,

which is characteristic of a vortex core region. However, working with experimental data and obtaining full knowledge of all spatial derivatives is both practically and computationally demanding. In the present study, stereoscopic particle image velocimetry data provide all three velocity components (u_1, u_2, u_3), but only in two spatial dimensions (x_1, x_2). This restricts the ability to calculate the derivative $\partial/\partial x_3$. To address this limitation, the two-dimensional approximation of the λ_2 field, as described by Schram et al. (2004) is used, defined as

$$\lambda_2 = \left(\frac{\partial u_1}{\partial x_1} \right)^2 + \left(\frac{\partial u_2}{\partial x_1} \right) \left(\frac{\partial u_1}{\partial x_2} \right). \quad (3.7)$$

The exact threshold value of λ_2 , which determines the limiting case of what is part of a vortex core and what is outside, is subject to some form of pragmatism. It is also worth mentioning that calculating the gradients of an experimental velocity field is prone to high levels of noise and inaccuracies. This was addressed by applying Gaussian blurring to the velocity field and calculating the gradient with a five-point central difference scheme. These measures and this parameter choice will be investigated and discussed further in Section 4.2.2.

3.5 Surface and sub-surface correspondence metrics

To quantify the performance of the wavelet-based detection method and the correlation between dimple detections at the surface and the vortices in the sub-surface flow region, a statistical measure is defined. Structures identified through the wavelet analysis of the surface reflections are referred to as *detections*. Suppose a vortex in the sub-surface plane, found with the method described in Section 3.4, is located within a search radius, r_s , directly beneath the detection. In that case, this is referred to as a *detection-vortex pair*. On the other hand, if no vortex is located below a detection, this event is classified as *no detection*. To quantify the proportion of detections that correspond to an underlying vortex, a metric termed the *match ratio* is defined as

$$\mathcal{M} = \frac{D_V}{D_V + D_N}, \quad (3.8)$$

where D_V is the number of all detection-vortex pairs and D_N denotes the sum of all detections with no vortex below. An important note here, illustrated in the top inset of Fig. 1.3, is that a single vortex may appear split into two regions where $\lambda_2 \leq \lambda_{2,\text{thr}}$. In such cases, when evaluating whether a detection has a vortex below and there are two vortices within the search radius, only one detection-vortex pair is counted.

For the analysis in Section 4.3.1, a similar metric is defined to quantify the proportion of vortices in the sub-surface plane that have a corresponding detection above them. This metric is defined as the *vortex match ratio*

$$\mathcal{V} = \frac{V_D}{V_D + V_N}, \quad (3.9)$$

where V_D is the number of vortices in the sub-surface region with a dimple directly above or within a search radius r_s , and the vortices without a corresponding dimple are denoted V_N .

Additionally, the two probabilities, $P[R_V]$ and $P[R_D]$ represents the likelihood of finding a match purely by chance. Specifically, $P[R_V]$ denotes the probability of finding a sub-surface vortex within a given search radius from an arbitrary surface position, and $P[R_D]$ is the probability of finding a surface detection within a given search radius from an arbitrary sub-surface position. These probabilities are based solely on the spatial coverage of detections or vortices and the search radius. They serve as reference baselines for evaluating the observed match ratios and assessing whether the match ratios exceed what would be expected by chance in Sections 4.3 and 4.4.

Chapter 4

Results and Discussion

In this chapter, the results obtained during the project are presented and discussed in the context of the objectives and research questions stated in Chapter 1. The chapter begins by describing the flow analysed in this project and the turbulent parameters relevant for the subsequent analysis. In Section 4.2, the parameter choices for both the wavelet-based detections of dimples and the identification of vortices in the sub-surface domain are discussed in terms of their impact on performance. Further, in Section 4.3, the results of detecting dimples through surface reflections and their correlation with sub-surface vortices are presented and discussed. In Section 4.4, the ceiling detections are benchmarked against the direct measurement of the surface using profilometry. Moreover, in Section 4.5, the number of detected dimples through profilometry and ceiling reflections is compared with the mean square horizontal divergence of the sub-surface flow. The chapter concludes with a summary of possible improvements and promising directions for future studies in Section 4.6.

4.1 Flow case and turbulent parameters

Using the LDV measurements and the methods presented in Chapter 2, the key turbulent parameters relevant to the flow analysis of this project are calculated and presented in Table 4.1. The Froude number is defined as $\text{Fr} = \sqrt{\bar{u}_1^2}/(2gL_\infty)^{1/2}$. Using the water temperature $\mathcal{T} = 19.2\text{ }^\circ\text{C}$, density is determined to be $\rho = 998.34\text{ kg/m}^3$. Along with the measured surface tension, $\sigma = 72.6\text{ mN/m}$, the Weber number is found to be $\text{We} = \rho\bar{u}_1^2L_\infty/2\sigma = 1$. In terms of the L, q diagram presented in Fig. 2.1, the flow considered in this project will fall near the border of Regions 0 and 3. It is noted that there are some significant discrepancies between the two LDV measurements, especially in the Taylor scale Reynolds number, Re_λ .

Table 4.1: Turbulent parameter values estimated using the LDV measurements conducted in the recirculating open water channel at NTNU, Trondheim. Details of these calculations are presented in Sections 2.1.2, 2.2 and 2.4

Depth	U_1 (m/s)	Fr	Re_∞	Re_λ	L_∞ (m)	λ_T (m)	L_v (m)	L_β (m)	T_∞ (s)
20 mm	0.2432	0.0161	1234	574	0.250	0.0232	0.0045	0.250	1.03
Bulk	0.2506	0.0146	1207	383	0.263	0.0167	0.0048	0.263	1.05

These discrepancies may be attributed to the fact that the LDV measurement closest to the surface lies within the surface-influenced region, illustrated in Fig. 2.4. A detailed analysis of these differences lies beyond the scope of this work, and for the analyses in the project, the bulk LDV measurements are used. Importantly, the variation between measurements has a negligible effect on the viscous layer thickness, L_v , which is the most relevant parameter for this study, as it serves as a key benchmark for comparing the present results with those of related studies, as discussed further in Sections 4.3 and 4.5.

4.2 Parameter tuning for dimple detection and subsurface vortices

The parameters for this analysis, discussed in Chapter 3, were partly selected based on pragmatic considerations. While these choices are physically grounded, a more rigorous optimisation of these parameters could further refine the detection method and yield slight improvements.

4.2.1 Dimple detection and tracking parameters

For the wavelet-based computer vision method used to detect dimples, several parameters needed to be defined and optimised. These include an appropriate scale, s , of the mother wavelet, the wavelet threshold, W_{thr} , and shape filtering parameters for detecting the relevant structures. Regarding shape filtering, the dimples to be detected were filtered based on eccentricity and solidity to identify the most circular structures, as introduced in Section 3.3. While the solidity threshold was somewhat arbitrarily set to $\mathcal{S} > 0.6$, it had no significant effect on the results. The solidity threshold was intended to filter out bent scars, which exhibit a circular shape. However, none of these were observed in the dataset. The absence of bent scars might be the result of the mean flow stretching out the structures in the longitudinal direction. Consequently, filtering for solidity will be more relevant for a flow with a weaker or absent mean flow, as observed by Babiker et al. (2023). There are other shape measures which could have been used, for instance, circularity. For the eccentricity, a threshold of $\mathcal{E} < 0.85$ was applied, consistent with the value recommended by Babiker et al. (2023) for effectively distinguishing dimples from other surface patterns. A more thorough inspection of the optimal eccentricity value would ideally require access to the surface velocity field, which is often impractical in an experimental setting.

The choice of wavelet scale s and wavelet threshold W_{thr} is interlinked. The wavelet transform will produce a peak in its signal when the wavelet matches the size of the feature in the signal. Additionally, the choice of scale influences the values of the wavelet transform. Based on the estimation of Froude and Weber numbers, presented in Table 4.1, the flow of interest is located on the border between Region 0 and Region 3 in Fig. 2.1. Given a Taylor microscale, $\lambda_T \sim \mathcal{O}(1 \text{ cm})$, it is reasonable to expect that the dimples, and therefore the wavelet scale, should be of a similar order of magnitude.

As shown in Fig. 4.1, multiple wavelet scales were tested, yielding broadly similar outcomes regarding the number of structures detected. Larger scales tend

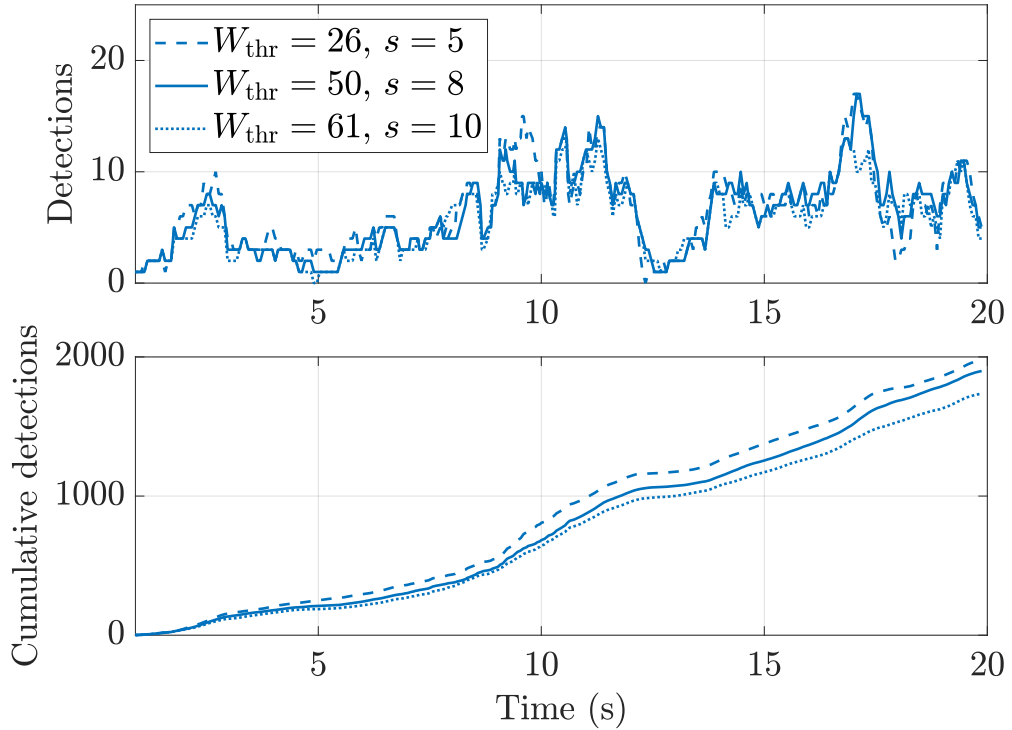


Figure 4.1: Dimple detection statistics for varying wavelet scales. **Top:** Number of detections per time step. **Bottom:** Cumulative detections. The results are shown for three different choices of the scale parameter s , each with a corresponding W_{thr} yielding a similar coverage rate across the scales. Detections are filtered by a minimum lifetime of $t_{\min} = 0.105T_\infty$.

to smooth out the curvature and miss the smaller features. In contrast, a smaller scale is more sensitive to the smaller features, including those associated with noise, which is reflected in the slight difference in cumulative detections across these scales. However, all choices more or less detect the same coherent structures. For the rest of the thesis, a scale of $s = 8$ is used. It is noted that in Fig. 4.1, the detections for different wavelet scales are presented for different values of W_{thr} . These thresholds were selected to yield a comparable detection coverage rate across scales. The reasoning behind this choice will be discussed in more detail later.

Another important note regarding the choice of scale and the results presented in this thesis is that the wavelet transform was conducted on a video with resolution 790×1127 pixels, where one pixel corresponds to < 0.5 mm at the surface. A Mexican hat wavelet with $s = 8$ has a diameter of 42.75 pixels, corresponding to approximately 15 mm in physical units. This scale effectively resolves most of the relevant dimples.

To determine an appropriate value of W_{thr} , the area coverage method proposed by Babiker et al. (2023) was used. Illustrated in Fig. 4.2 is the total coverage plotted as a function of W_{thr} . The threshold used in the analysis is chosen at a point where this coverage curve begins to level off, reducing sensitivity to small changes in this parameter and ensuring a robust detection. At $W_{\text{thr}} = 50$, the initial coverage is approximately $\approx 0.4\%$ prior to shape filtering. After filtering, the coverage is $\approx 0.25\%$, similar to the area coverage used by Babiker et al. (2023). This choice of threshold limits the detections strictly. However, it leads

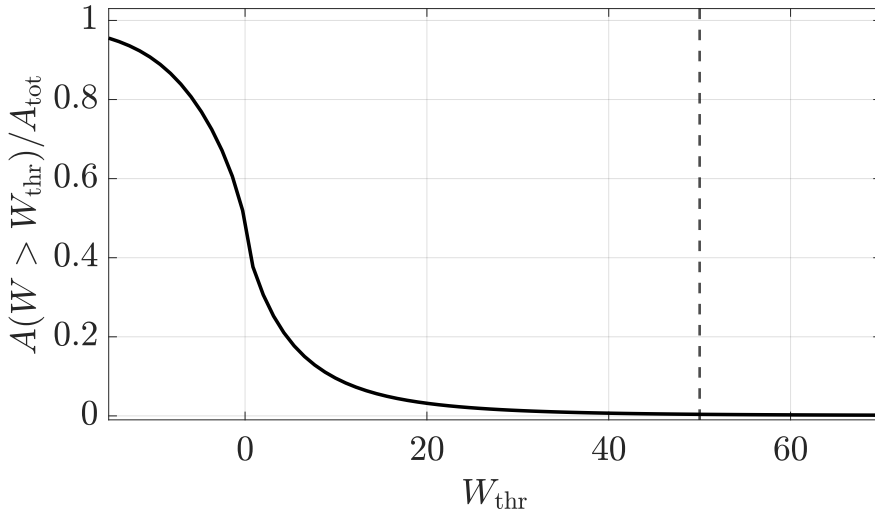


Figure 4.2: Fraction of the wavelet transformed surface reflection signal with wavelet coefficient exceeding the threshold W_{thr} . The dashed vertical line at $W_{\text{thr}} = 50$ indicates the threshold value used for the analysis in this project, at which the coverage rate is approximately 0.4% before shape filtering.

to a stable match ratio, defined in Section 3.5 as the fraction of detections in the surface reflections with a vortex underneath, divided by the total number of detections.

A perfectly optimal choice of W_{thr} is unlikely to exist, and the results presented in this thesis should be interpreted with this limitation in mind. As illustrated in Fig. 4.3, when imposing lifetime threshold $t_{\min} = 0.105T_{\infty}$ and a search radius $r_s = 0.59\lambda_T$, the match ratio, \mathcal{M} , increases with increasing values of W_{thr} . The rationale behind the search radius is more thoroughly described in Section 4.3. The increase in \mathcal{M} likely reflects that a stricter threshold excludes false positives and retains more accurately detected dimples. However, the increase in match ratio comes at the cost of the number of detected matches as fewer dimples are detected with a higher W_{thr} . On the other hand, for a too low W_{thr} , the detection seems to be overly sensitive towards small disturbances at the surface, even after lifetime filtering. In other words, a threshold that is too low includes noise, and a threshold that is too high excludes real dimples. Striking the perfect balance is very difficult.

The value of $W_{\text{thr}} = 50$ is chosen based on total area coverage, as discussed above, and a value where the matching accuracy as a function of W_{thr} plateaus, as shown in Fig. 4.3. It is recognised that such a strict threshold might exclude some real dimples from the analysis. Nonetheless, in the comparison between surface reflections and direct measurements via profilometry, discussed in Section 4.4, the threshold value is chosen similarly for the profilometry data.

4.2.2 Vortex core detection

Although Jeong and Hussain (1995) defines vortex cores as regions where $\lambda_2 < 0$, it is necessary to use a stricter criterion for the analysis in the current project. Since the whole three-dimensional velocity field is not available, the two-dimensional

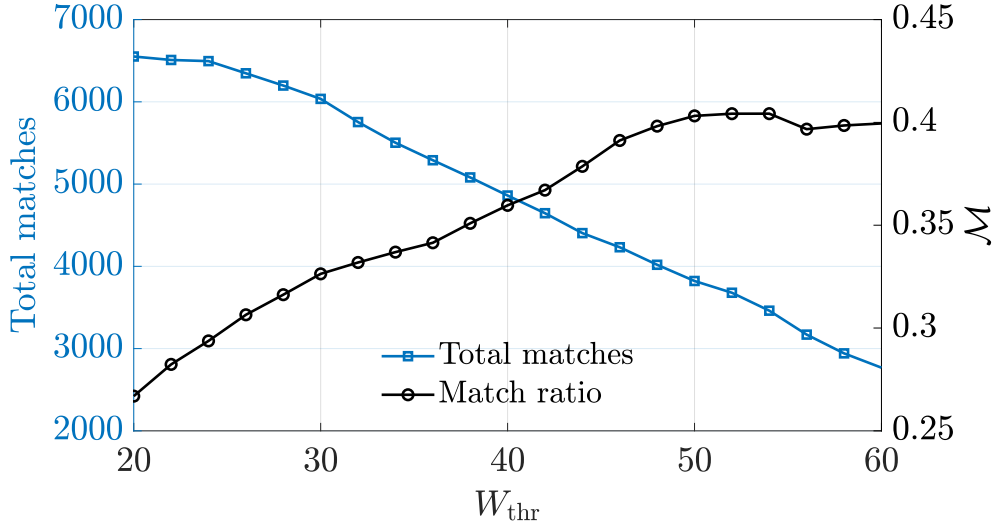


Figure 4.3: Detected dimples and match ratio as a function of W_{thr} . The blue line (left axis) shows the number of dimples detected in the surface reflections with a vortex core underneath. The black line (right axis) represents the match ratio. These results are presented for a minimum track lifetime of $t_{\min} = 0.105T_{\infty}$ and a search radius of $r_s = 0.59\lambda_T$.

approximation of the λ_2 criterion, as introduced in Section 3.4, is used. When the threshold value $\lambda_{2,\text{thr}}$ is set too liberally, an excessive number of vortices are detected.

To address the choice of $\lambda_{2,\text{thr}}$, the probability density function of the non-dimensionalised λ_2 values, calculated with Eq. (3.7), is examined, as shown in Fig. 4.4. The distribution is centred around zero, and by choosing a threshold value at a point where the probability density function flattens out, a solid separation between regions dominated by swirling is ensured. The mean and standard deviation are calculated, accounting only for the negative values. The dashed line in Fig. 4.4 represents the chosen threshold value, $\lambda_2\lambda_T^2/\bar{u}_1'^2 = -3.03$, which corresponds to approximately two standard deviations below the mean of the negative portion of the distribution. This threshold value is consistent with the limit proposed by Schram et al. (2004). A different approach, which yields approximately the same results, is to impose a more liberal $\lambda_{2,\text{thr}}$ and discard vortices below a minimum area.

To reduce the influence of noise and sharp gradients, Gaussian blurring is applied to the velocity fields before computing the gradients. The blurring is performed using one standard deviation of blurring and a smoothing kernel of 3×3 pixels. Another noise-reducing measure employed was the use of a five-point central difference scheme in calculating the spatial gradients.

An example of the vortex core detection is shown in Fig. 4.5 where the detected vortex cores are encircled. The insets show a detailed view of three of these vortices. For the value of $\lambda_{2,\text{thr}}$ utilised, approximately 130000 vortices are detected across the 3600 timesteps of the SPIV dataset. A key point to note is that this field addresses the vertically oriented swirling motion. At this depth, $d \approx 2L_v$, the vorticity exhibits less directional preference compared to closer to the surface, a matter introduced in Section 2.3. In other words, there are more vortices present

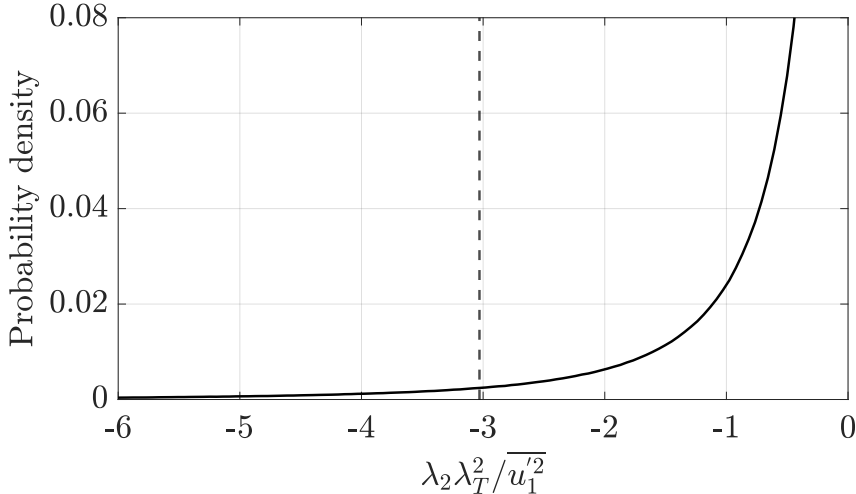


Figure 4.4: Probability density function of the λ_2 fields from the entire dataset normalised by the square of the Taylor microscale and the variance of the velocity fluctuations. The dashed vertical line at $\lambda_2 \lambda_T^2 / \bar{u}_1'^2 = -3.03$ represents the threshold value used for vortex core identification in this project.

in the flow than what is caught by the λ_2 criterion.

4.3 Surface reflection detections as imprints of sub-surface vortices

Once all the parameters for the detection of dimples and for finding vortices in the sub-surface region are set, one of the research questions raised in Chapter 1 can be addressed: the extent to which structures detected in the surface reflections correspond to vortices beneath the surface. Before initiating the proper analysis, some assumptions are made about the dimple detections. Recalling the long-lived nature of dimples, introduced in Section 2.4, filtering the detections for a minimum lifetime effectively removes some of the noisy artefacts of the surface reflections, which are assumed to be related to short-lived surface disturbances. The top panel of Fig. 4.6 shows the number of dimple tracks as a function of the non-dimensional lifetime t_{\min}/T_∞ . A key observation is that the majority of tracks last for only one timestep and that the steep decrease plateaus slightly around $t_{\min}/T_\infty \approx 0.1$. Imposing a stricter lifetime threshold yields diminishing returns and likely removes true dimples along the way.

On the other hand, as observed in the bottom panel of Fig. 4.6, the impact of the lifetime threshold on the match ratio is small. Even when the shortest-lived detections are included, the match ratio remains similar to values obtained for stricter filtering. The relatively small impact on \mathcal{M} suggests two things: first, that a threshold $W_{\text{thr}} = 50$ seem to be able to detect dimples and not many noisy artefacts, and second, that many dimples lie around the threshold value and can be lost and reappear, causing them to be falsely discarded by the lifetime filtering.

Based on this analysis, setting $t_{\min} = 0.105T_\infty$ does yield a relatively high \mathcal{M} while still including many detections. It is expected that the lifetime threshold

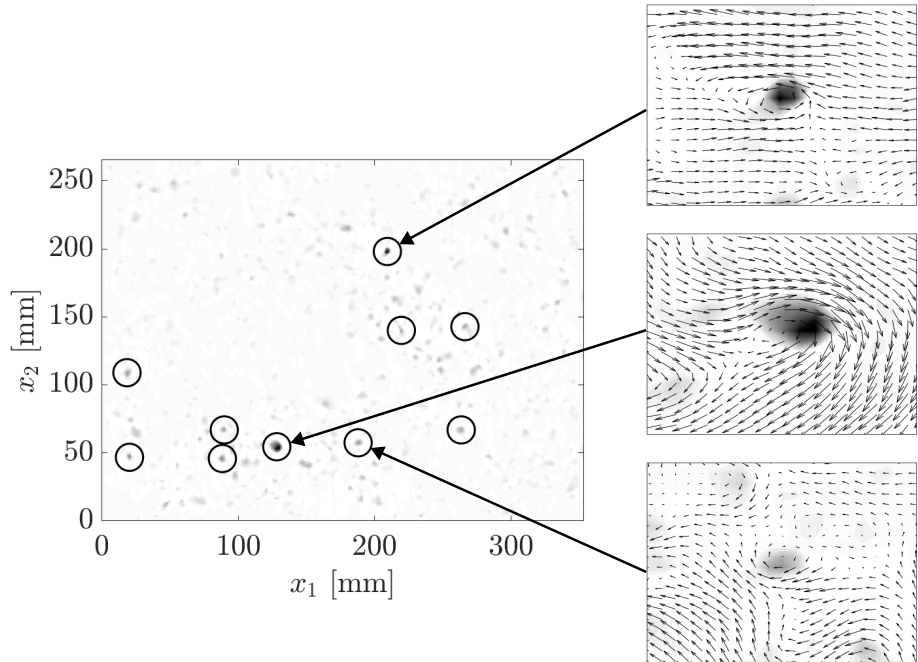


Figure 4.5: Visualisation of the λ_2 field at a single timestep with regions where $\lambda_2 < \lambda_{2,\text{thr}}$ indicate potential vortex cores. Insets show detailed views of three selected vortex candidates, with local velocity field vectors superimposed onto the λ_2 contours for enhanced clarity. The mean flow, U_1 , has been subtracted for visualisation purposes.

would play a more significant role for a less strict choice of W_{thr} as it is observed that this tends to include larger numbers of non-dimple detections.

A conceptual illustration of the lifetime-filtered dimple detections compared with the vortex cores identified in the λ_2 field at a depth $d = 10$ mm is shown in Fig. 1.3. There, the surface reflections are mapped onto the surface coordinates. For that specific timestep, there is a strong correspondence between the dimples and vortices. Notably, there are weaker circular regions in the reflection plane that are not detected as dimples, and there are dark areas, representing $\lambda_2 < 0$, not identified as vortices in the sub-surface region. This is a direct consequence of the thresholding criteria discussed in Section 4.2. For the timestep shown in Fig. 1.3, the match ratio is $\mathcal{M} = 0.75$.

Under the flow conditions in this experiment, the viscous layer thickness is estimated to be $L_v \approx 5$ mm, meaning that the sub-surface plane of SPIV is at a depth $d \approx 2L_v$. This depth puts a natural restriction on the expected correspondence between dimples at the surface and vortices directly below. Even though vertically oriented vorticity, ω_3 , attached to the surface is persistent both in time and highly correlated spatially throughout the viscous layer (Shen et al., 1999, §6.2), this correlation decreases with increasing distance from the surface. An explanation of this is the interaction of vorticity with the surface. As discussed in Section 2.3, vorticity cannot end within the fluid; it must either form closed loops or attach to boundaries. A conceptual illustration of this principle is shown in Fig. 4.7, where a vortex loop is depicted after surface attachment. Due to variations in vortex strength and size, not all of these loops penetrate the fluid equally deeply after

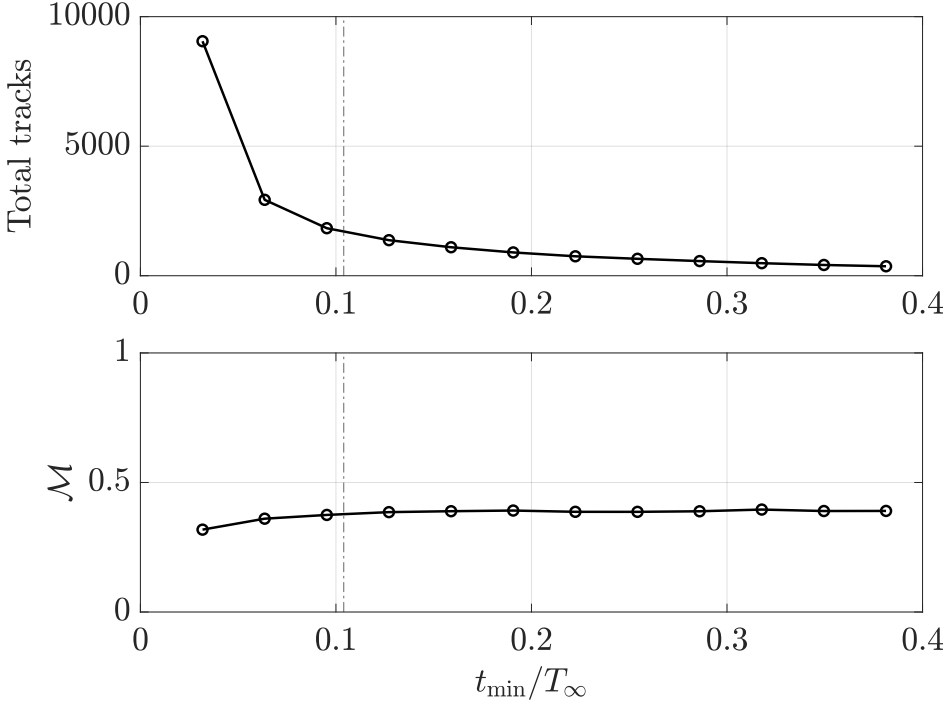


Figure 4.6: **Top:** All detection tracks from surface reflections plotted as a function of minimum lifetime, t_{\min}/T_∞ . **Bottom:** Match ratio as a function of the track lifetime. Results are shown for a search radius of $r_s = 0.59\lambda_T$.

attachment. This provides a physical explanation for why a perfect one-to-one correlation between surface dimples and sub-surface vortices cannot be expected at this depth.

In a related study, through their investigation of dimples and sub-surface vortices Aarnes et al. (2025) found that the probability of being inside a vortex core at a depth $d = 2L_v$ is ≈ 0.75 in direct numerical simulations (DNS) with no mean flow present. However, such a high correspondence is not expected in the present study. Unlike DNS, the experimental data is limited in both spatial and temporal resolution, which reduces the precision with which the sub-surface velocity and vorticity fields can be resolved. Additionally, as noted in Section 2.1.2, Aarnes et al. (2025) defines the integral length scale, L_∞ , in a different way than what is used in the present study. As the viscous layer depth is defined as $L_v = 2\text{Re}_\infty^{-1/2}/L_\infty$, the differences in integral scales might lead to differences in L_v . These deviations are likely small, but highlight the point made in Section 2.1.2, that the turbulent parameters should be regarded as estimations, not exact values. Consequently, the match ratio observed in this study should be interpreted in light of these experimental constraints and methodological differences.

Another source of uncertainty related to the experimental data arises from the spatial and temporal calibration of the surface reflection plane and the sub-surface velocity field. Spatially, manual calibration with the sub-surface plane introduces some uncertainty, as discussed in Section 3.1.2. However, the calibration was performed on a small portion of the data, and the match ratio remains largely unchanged even when this part of the data is omitted. Temporally, the two time series are not synchronised. As a solution to this problem, when comparing the two planes, the reflection detections are advected according to the time difference

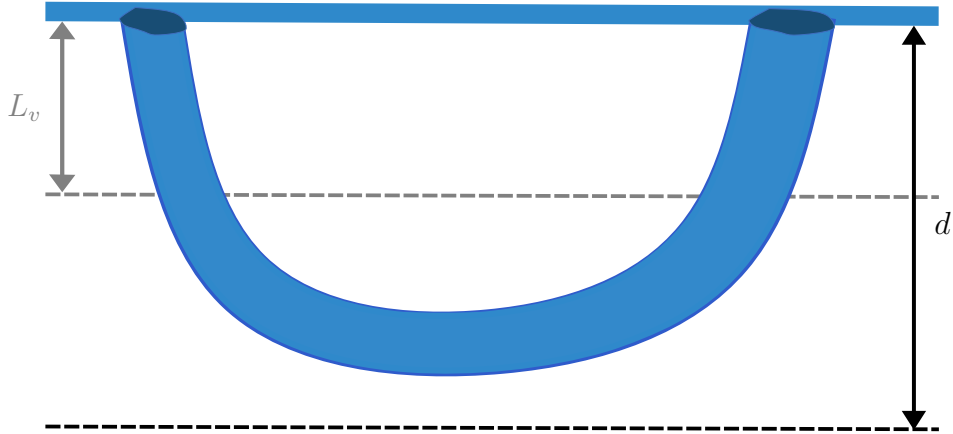


Figure 4.7: Schematic of a vortex loop following surface attachment. Two counter-rotating surface dimples represent the attached segments of the vortex, connected beneath the surface by a horseshoe-shaped structure. This configuration demonstrates that not all attached vortices extend deeply into the flow, explaining why a sub-surface vortex core is not necessarily found directly beneath its surface attachment position.

from the corresponding SPIV time step and the mean flow. While this advection improves temporal alignment, it cannot fully account for the fact that the instantaneous velocity, Eq. (2.4), differs slightly from the assumed mean.

Therefore, in light of the mentioned uncertainties and experimental limitations, a search radius r_s is imposed when searching for corresponding dimple-vortex pairs. The approach taken here diverges slightly from the method of Aarnes et al. (2025), who defined matches based on the centroid of the detected dimple and compared this to regions where $\lambda_2 \leq \lambda_{2,\text{thr}}$. In the present study, a sub-surface vortex is defined similarly as regions where $\lambda_2 \leq \lambda_{2,\text{thr}}$. However, a *detection-vortex pair* is defined as a case where the centroid of the detection lies directly above the centroid of the vortex or within the specified search radius r_s .

The match ratio as a function of the search radius is presented in Fig. 4.8. As expected, \mathcal{M} increases with a larger r_s . For a value of $r_s = 0.59\lambda_T$, a radius which is representative of expected dimple sizes and large enough to help partially overcome, though not eliminate, the calibration uncertainty, the match ratio $\mathcal{M} \approx 0.39$. While this match ratio is notably lower than what is observed with DNS data, it is still significantly higher than the probability of finding a sub-surface vortex from an arbitrary point at the free surface. An even larger difference between \mathcal{M} and the random search will be discussed in Section 4.3.1. The method used by Aarnes et al. (2025) would likely yield a slightly lower \mathcal{M} , as smaller vortices are given the same weight in terms of search radius in the present study. This simplification may lead to false matching, where a dimple is matched to a nearby but unrelated sub-surface vortex. An alternative option, as mentioned in Section 4.2.2, is to impose a minimum area for the definition of vortices in the sub-surface region. However, this restriction yields similar results in terms of \mathcal{M} as those observed in Fig. 4.8, indicating limited benefit in terms of overall matching performance.

Another factor to consider when evaluating the accuracy of the surface reflection detections is the optical and scattering properties of the surface. Due to

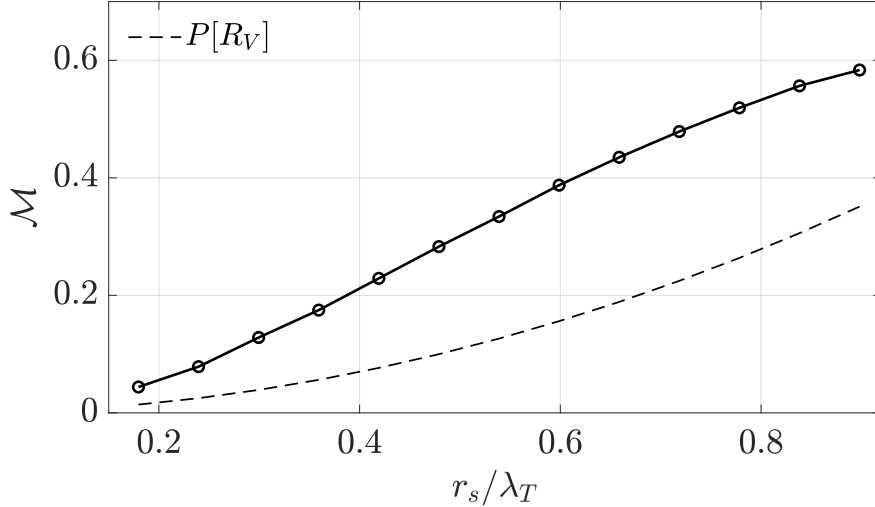


Figure 4.8: Match ratio as a function of search radius, r_s for minimum lifetime $t_{min}/T_\infty = 0.105$. The dashed line indicates the probability of detecting a vortex below a random position at the surface, shown as a function of r_s .

these effects, the brightest regions do not necessarily correspond to the strongest dimples. The brightness of the dimples mainly relies on the focal plane, the plane where the light rays converge, of the given indentation and the distance from the surface to the projector screen. The brightest dimples are those whose focal plane aligns closely with the plane of the projector screen. For future replications of this experiment, a movable projector screen is recommended to enhance the robustness of dimple detection. While the current setup performs well, a deeper investigation into the curvature of the dimples and the optimal distance to the projector screen could further improve detection consistency. As Babiker et al. (2023) points out, dimples are relatively uniform in size, making it likely that their focal points are also quite similar.

4.3.1 Impact of sorting sub-surface vortices by lifetime

Until this point, no other restriction than $\lambda_2 \lambda_T^2 / \bar{u}_1'^2 \leq -3.03$ is put on the definition of vortex cores. However, using the same method as for restricting reflection detections by lifetime, the vortices can be filtered in a similar manner. The motivation for introducing this criterion is to investigate whether this serves as a more robust comparison between detections and vortices. As discussed in Section 4.3, there is a possibility that a matching pair of detections and vortices is false in the sense that these two do not belong to the same vortex structure. To address this, the same lifetime filter for the sub-surface vortices, $t_{min,subsurface} = 0.105 T_\infty$, is applied to the sub-surface vortices. The effect of this filtering is presented in Fig. 4.9. Compared to the instance where all vortex detections are kept, the filtering results in a lower absolute match ratio, which is reduced by 6.8%. This decrease is relatively modest compared to the 21% decrease in vortices to match against, which implies that removing the short-lived vortices leads to a larger difference between M and $P[R_V]$. First, this suggests that the short-lived vortices are less likely to be attached to the surface, in line with the theory introduced in Section 2.3. Sec-

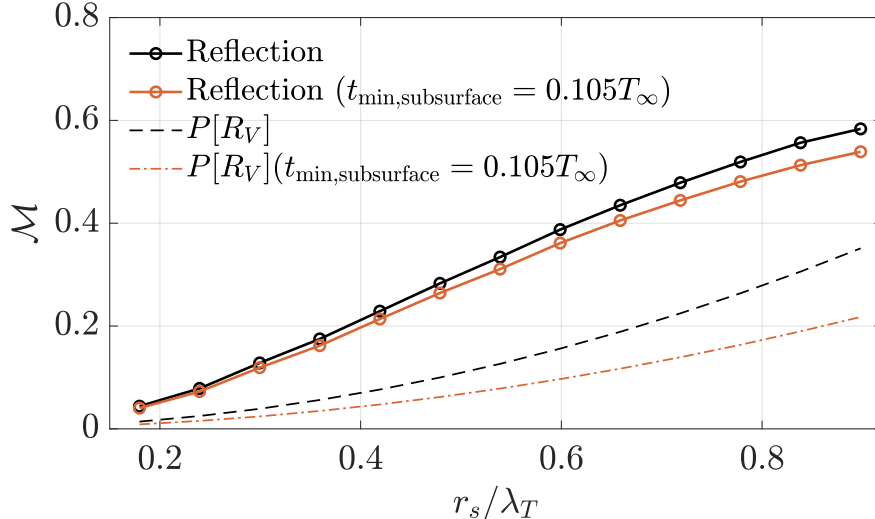


Figure 4.9: Match ratio, \mathcal{M} , as a function of the search radius for the surface reflection detections. The black lines represent \mathcal{M} and $P[R_V]$ where all sub-surface vortices are included, $t_{\min,\text{subsurface}} = 0$. The orange lines show the same surface detections, but compared to vortices in the sub-surface region filtered for a minimum lifetime, $t_{\min,\text{subsurface}} = 0.105T_\infty$. In both cases, the surface detections are filtered for a minimum lifetime of $t_{\min} = 0.105T_\infty$.

ond, this filtering may help eliminate some of the false-positive detection-vortex pairs, thereby robustifying the comparison of the planes. While some real vortices are excluded through this filtering, these are likely not the coherent structures of interest when investigating surface dimples.

Another observation regarding filtering sub-surface vortices for a minimum lifetime is related to the vortex match ratio. As introduced in Section 3.5, it is the probability of finding a dimple detection directly above an identified vortex. As presented in Fig. 4.10, \mathcal{V} is plotted as a function of the vortex lifetime threshold, $t_{\min,\text{subsurface}}/T_\infty$. The value of \mathcal{V} is significantly lower than what is observed for \mathcal{M} , underlining the fact that there are far more vortices in the sub-surface region than dimples at the surface. This observation is influenced by both the method used for detecting and defining dimples and vortices in the current project and the general observation that the level of vorticity is higher outside the viscous layer (Shen et al., 1999).

However, \mathcal{V} increases as a function of $t_{\min,\text{subsurface}}/T_\infty$, suggesting that the longest living vortices are more likely to be connected to the dimples observed at the surface. Compared to $P[R_D] = 0.0213$, illustrated by the dashed line in Fig. 4.10, there are more dimples above the long-lived vortices. There is no proper ground truth to compare against here. Still, the value of \mathcal{V} is likely lower than the theoretically expected value for the same reasons as discussed with the match ratio in Section 4.3. The same problem as with detections in surface reflections, where structures are lost and then found again, also affects the value of \mathcal{V} after lifetime filtering.

One interesting observation is that the longest-lived vortices appear to correspond more closely to the dimples than to the shorter-lived vortex structures. This trend is as expected from the theory that surface-attached vortices are more

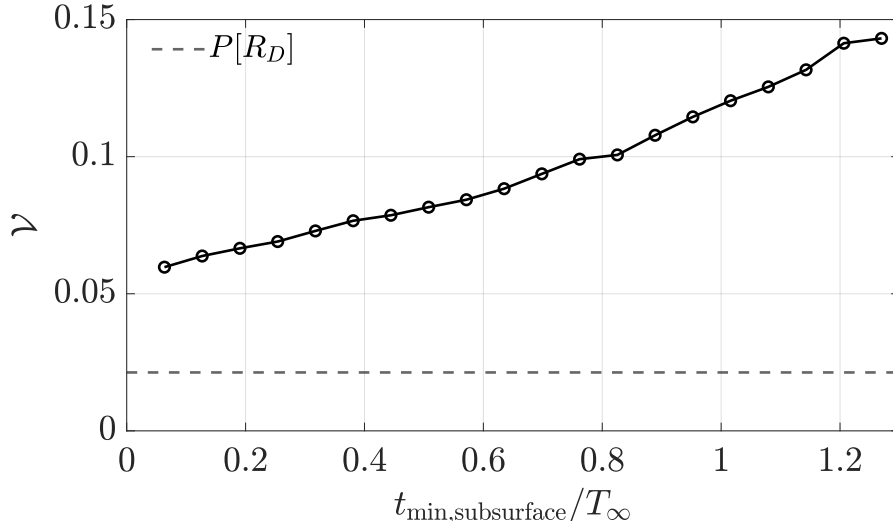


Figure 4.10: Vortex match ratio, \mathcal{V} , as a function of sub-surface vortex lifetime. A fixed search radius, $r_s = 0.59\lambda_T$, is used. The dashed line represents $P[R_D]$, the probability of a dimple detection being directly above, or within r_s , of an arbitrary position in the sub-surface plane.

persistent than other structures, and the experiments indicate the same pattern. However, for a $t_{\min,\text{subsurface}}/T_\infty$ larger than one, the vortices analysed are those that travel through the entire domain, and this number is relatively small for this dataset.

4.4 Comparison of surface reflection dimple detection with direct profilometry measurements

This section is devoted to comparing the performance of dimple detections using surface reflections with that based on direct surface elevation measurements using Fourier transform profilometry (FTP), one of the main research questions defined in Chapter 1. As mentioned in Section 3.1, a detailed description of the methodology behind the profilometry acquisition is beyond the scope of this project; for a comprehensive review, see X. Su and Chen (2001). The profilometry dataset consists of 10800 frames of surface elevation profiles sampled at 45 Hz. Contrary to the surface reflection data, this plane is already spatially aligned with the SPIV field. Although the profilometry is sampled at three times the frequency of the SPIV, the two datasets have synchronised samplings. Every third frame of the profilometry aligns with every SPIV frame. A slight time lag of $dt \approx 11.2$ ms exists between these aligned samplings, corresponding to an offset of $U_1 dt \approx 2.5$ mm. This time lag is not accounted for in the analysis. However, it is unlikely to significantly impact the results due to the imposed search radius when comparing dimple detections and sub-surface vortices. This uncertainty is of the same order as the uncertainty from the ceiling reflection coordinate calibration.

For dimple detection in the profilometry, the same reasoning behind wavelet parameter choices is applied as discussed in Section 4.2. One key difference is that the regions of interest are now corresponding to the lowest values, such that the

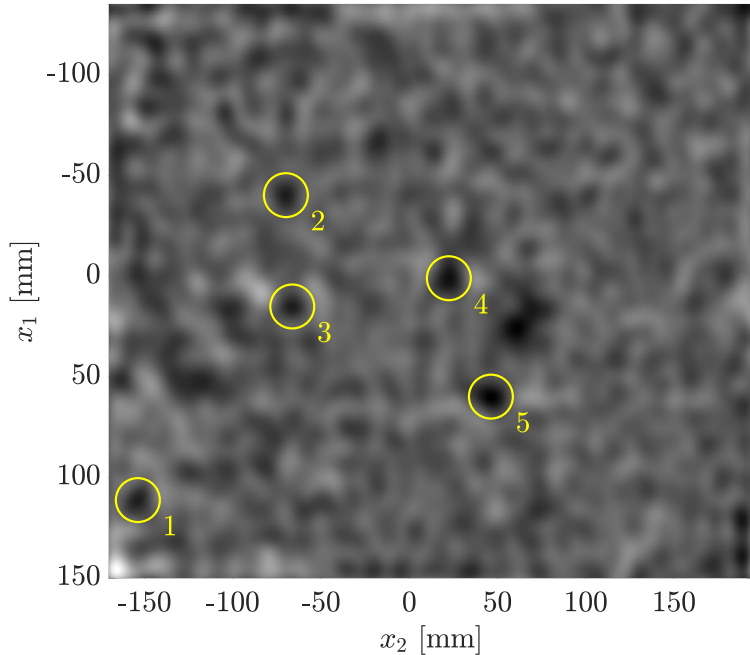


Figure 4.11: Example snapshot of the wavelet transform applied to the profilometry data. Encircled regions indicate detected and tracked dimples where $W < W_{\text{thr}}$.

dimples are found by selection $W < W_{\text{thr}}$. Although the surface elevation field could have been inverted to follow the same convention as described in Fig. 3.2, doing so would have yielded the same results. For the analysis, $W_{\text{thr}} = -0.2$ is used.

The choice of wavelet scale for the profilometry differed slightly from the process described in Section 4.2.1. An example snapshot of the wavelet-transformed profilometry data is shown in Fig. 4.11, where it is observed that a significant amount of noise is present in the profilometry data, even after applying the wavelet transform. These levels of noise influenced the choice of the appropriate s . The grid size of the profilometry is 433×548 , and the field of view is $288 \text{ mm} \times 365 \text{ mm}$, yielding a spatial step size of $\approx 1.5 \text{ mm}$. For the example shown in Fig. 4.11 and the following analysis, a wavelet scale of $s = 8$ was used. Physically, this corresponds to a wavelet of diameter $\approx 60 \text{ mm}$, substantially larger than the dimples we expect to detect at the surface. Based on the argumentation for scale choice in the reflection detections in Section 4.2.1, a smaller scale, $s = 2$ or $s = 3$, would have been more sensible. However, at such low scales, the noise in the profilometry field overwhelmed the signal of the dimples, making robust detection impossible. The choice of $s = 8$ for the profilometry blurs out some of the noisy features, allowing for the detection of the strongest and most coherent signals. While this scale improves robustness, it likely eliminates some of the smaller or short-lived dimples at the surface, a point that will be revisited in the following paragraph.

The noisy nature of the profilometry is also apparent in the top panel of Fig. 4.12 where the total number of tracks is plotted as a function of t_{\min}/T_{∞} . Compared to the reflection detections, the profilometry data has a significantly higher number of tracks that only live for one time step. This suggests that many

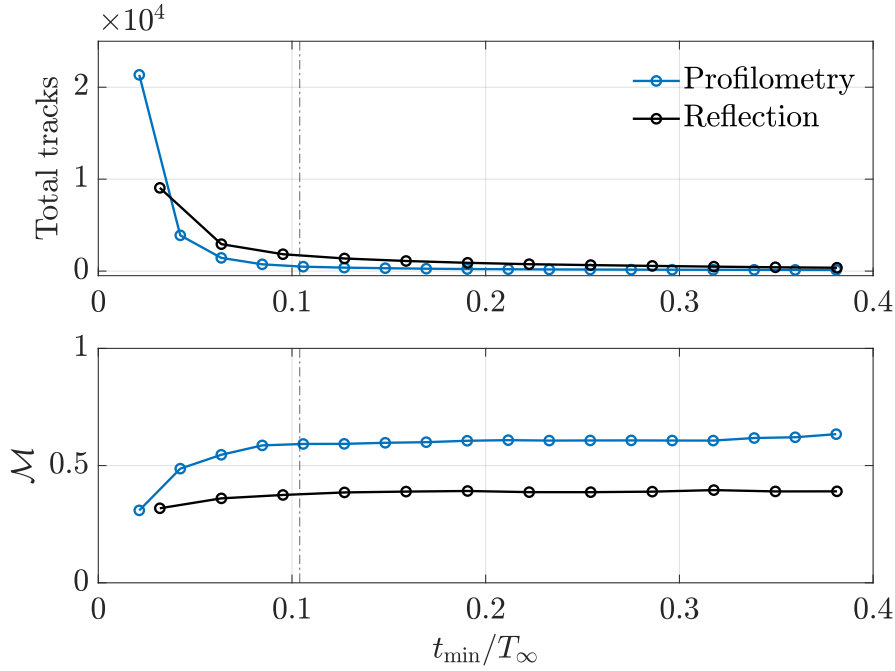


Figure 4.12: **Top:** All detected tracks from surface reflections and profilometry plotted against minimum lifetime, t_{\min}/T_∞ . **Bottom:** Match ratio, \mathcal{M} , as a function of minimum track lifetime. A search radius of $r_s = 0.59\lambda_T$ is used for all results. The dash-dotted vertical line indicates $t_{\min}/T_\infty = 0.105$.

of these detections are the result of noise rather than true dimples. Additionally, compared to the reflections, significantly fewer tracks are detected in the profilometry once a minimum lifetime of $t_{\min} = 0.105T_\infty$ is imposed. This can be attributed to two factors. First, the noise causes many tracks to get lost and found again, resulting in a wrongfully short lifetime for some tracks. Second, the choice of $s = 8$ blurs out some real dimples that might be smaller or short-lived, as discussed above.

The bottom panel of Fig. 4.12 further supports the hypothesis that the short-lived detections in the profilometry are due to noise. Specifically, the match ratio, \mathcal{M} , increases significantly as the lifetime threshold grows from $t_{\min} = 0$ to $t_{\min} = 0.105T_\infty$. This trend is not observed in the same way for the ceiling detections, suggesting that there are fewer noise-related detections in that dataset. The same plateau is observed for \mathcal{M} as t_{\min} increases in both datasets, implying that the correspondence between surface detections and sub-surface vortices is independent of dimple lifetime, as long as the shortest-lived structures are excluded.

It is also worth noting that, in this analysis, the vortices in the sub-surface region are not filtered for a minimum lifetime. As discussed in Section 4.3.1, this filtering has a small effect of \mathcal{M} for the surface reflections. A similar trend is observed for the profilometry-based detections, meaning that this does not significantly impact the performance of these two methods compared to each other.

The key observation from this analysis is that in terms of \mathcal{M} , profilometry-based dimple detection outperforms surface reflections. This result is expected, given that the profilometry provides both a direct measurement of the surface with an aligned coordinate system, resulting in less uncertainty. Image distortion, optical errors, and calibration uncertainties contribute to reduced accuracy for

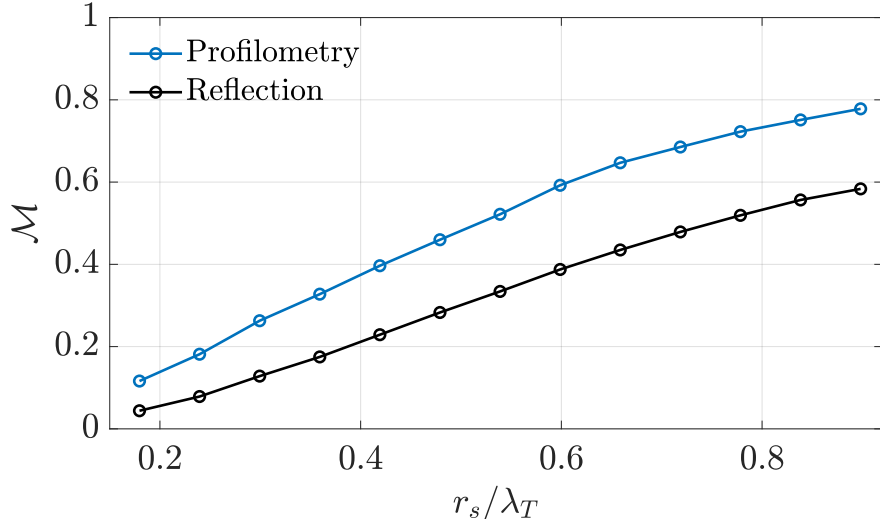


Figure 4.13: Comparison of match ratios as a function of search radius for profilometry and surface reflection data. A minimum lifetime of $t_{\min} = 0.105T_\infty$ is applied for these results.

the reflection detections. The same trend is observed in Fig. 4.13, that the profilometry is consistently detecting a higher \mathcal{M} for different search radii. However, as pointed out earlier, due to the relatively large wavelet scale used in the profilometry analysis to mitigate the noise, far fewer dimples were detected compared to the reflection detections. At a search radius of $r_s = 0.59\lambda_T$, the match ratio is $\mathcal{M} = 0.388$ for the reflection detections and $\mathcal{M} = 0.592$ for the profilometry. However, despite the higher match ratio, the profilometry data yielded only 1073 detection-vortex pairs, compared to 3596 for the surface reflection data at this search radius. These numbers support the hypothesis that only the most prominent dimples are detected in the noisy profilometry data. This could imply that the match ratio for the profilometry is artificially high, as fewer but more distinct dimples are included in the analysis. As observed in Fig. 4.13, the match ratio increases to the value observed with DNS by Aarnes et al. (2025) as r_s approaches λ_T . Firstly, this large r_s is likely to include some false matches. Secondly, as discussed above, not all dimples are detected, which affects the match ratio somewhat and should be taken into account when interpreting these results.

Even though the profilometry data fails to detect all dimples and has some weaknesses, it serves as an important benchmark for the reflection-based detection method. The fact that both methods yield comparable results strengthens confidence in the reflection-based approach. Moreover, the dimples appear to carry more meaningful information about the sub-surface flow, which will be explored further in Section 4.5.

4.5 Dimple detections and sub-surface horizontal divergence

As stated in Section 1.4 and the research questions, one of the aims of this thesis is to investigate the relationship between surface reflection observations and the

flow in the sub-surface domain. As shown in earlier sections of Chapter 4, a clear relation exists between the observation of dimples in the surface reflections and the probability of finding a vortex in the vicinity of this spatial coordinate below the surface. However, as this may have promising applications for sub-surface flow reconstruction, this section shifts focus towards the number of observed dimples, $N(t)$ and its relationship with the mean square horizontal divergence in the sub-surface velocity field.

There is a well-established relationship between sub-surface turbulence and gas transfer rates across the air-water interface, as introduced in Section 1.1. More specifically, it is shown to be a clear connection between the gas transfer rates, surface renewal and root-mean-square surface divergence, $\beta(t)$ (Herlina and Jirka, 2008; Veron et al., 2011). Building on this, Babiker et al. (2023) shows that the number of attached dimples $N(t)$ lags $\beta(t)^2$ by $0.8T_\infty$. This finding highlights the potential to estimate gas transfer rates simply by counting dimples at a free surface.

With this context in mind, it is of particular interest to investigate how the number of dimples detected through the surface reflections correlates with the mean square horizontal divergence in the sub-surface flow. While this does not directly represent the surface divergence, it is likely still linked to surface renewal processes and gas transfer at the air-water interface. As defined in Section 2.2, the sub-surface horizontal divergence reported in this project is denoted $D_h(t)^2$ to avoid confusion with the surface divergence reported by aligning studies.

Figure 4.14 shows the time series of the mean square horizontal divergence $D_h(t)^2$ and the number of detected dimples from both the profilometry and surface reflections dataset, for the first 20 seconds of the analysed datasets. For visual clarity, the detection counts are shown as a running average over $0.32T_\infty$. Although this represents a relatively short segment of the full time series, and is insufficient for drawing definitive conclusions, it is evident that all three time series fluctuate similarly, moving up and down together, suggesting a connection between these quantities. As discussed in Section 4.4, the number of dimples detected in the profilometry data is consistently lower than in the surface reflections. It is noted that the surface reflection video has a significantly larger field of view compared to the two other datasets. However, for a fair comparison, only detections in regions overlapping with the SPIV field of view are included in the reported detection counts.

One notable anomaly in Fig. 4.14 occurs around $t = 10$ s, where the $D_h(t)^2$ is steadily high for an extended period without the same trend in the number of detections. This exception highlights one of the challenges of conducting this analysis in the presence of a mean flow. During this interval, many upwelling events appear to pass through the domain, consistent with the persistently high $D_h(t)^2$. However, the number of detected dimples for this event only has a short-lived spike. As Banerjee (1994) notes, dimples appear along the edges of upwelling boils, and the dimples lag the surface divergence (Babiker et al., 2023). In the current experiments, with a mean flow, vortices and dimples are advected downstream, as discussed in Sections 2.1.2 and 2.3. As a result, many of these dimples may move out of the field of view before or shortly after forming, which limits the reliability of dimple counts as an indicator of sub-surface activity.

To investigate this relationship further, the normalised cross-correlation be-

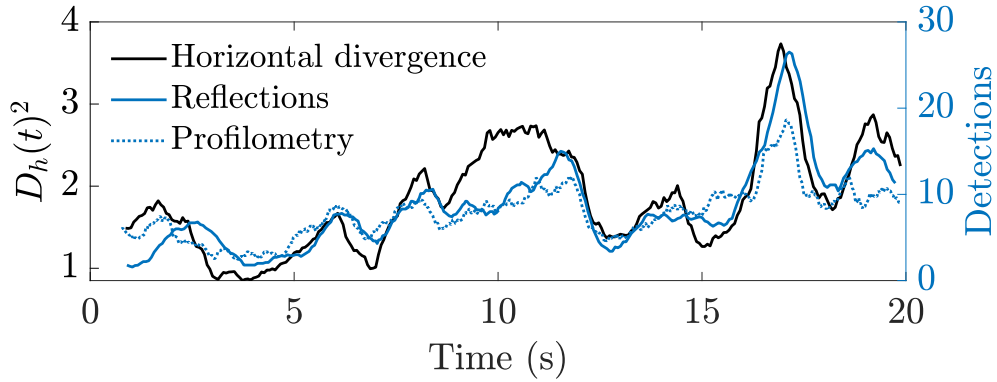


Figure 4.14: The time series of dimple detections obtained from both surface reflections and profilometry, plotted alongside the mean square horizontal divergence in the sub-surface velocity field. The dimple detections are presented as a running average with a window of $t = 0.32T_\infty$.

tween the time series of the mean square horizontal divergence $D_h(t)^2$ and the number of detected dimples was calculated. A running average with a window of $0.32T_\infty$ was used for all three datasets to mitigate some of the noise, particularly related to the dimple count. For this analysis, only dimple tracks with a lifetime exceeding $t_{\min} = 0.105T_\infty$ are included. However, it is noted that a similar correlation pattern emerges even without filtering for a minimum lifetime.

As shown in Fig. 4.15, a clear correlation is observed between the number of detected dimples and the mean square horizontal divergence at a depth of $d = 10$ mm. The correlation peaks at a time lag of approximately $0.06T_\infty$ for the profilometry data and around $0.13T_\infty$ for the surface reflection data. The difference in the observed time lag between the two datasets is small. It is likely the result of the significantly lower number of dimples detected in the profilometry dataset, which may affect the statistical robustness of the correlation, as many real dimples are left undetected. Alternatively, the difference could come from uncertainties in the time calibration of the surface reflection video. The same factors may also explain the slightly higher peak correlation observed for the reflection detections, suggesting a somewhat closer relationship between these detections and the sub-surface horizontal divergence.

The peak in the cross-correlation for the reflection data is approximately 0.4, indicating a moderate but not particularly strong correlation. This suggests that, although the surface divergence is observed to have a strong correlation with dimple detections, this correlation is weaker at a depth of two viscous layers. This outcome is both expected and interesting, and it invites further investigation into the connection between divergence at varying depths, a point that will be revisited later.

It is worth noting from Fig. 4.15 that the time lag between surface divergence and dimple count reported by Babiker et al. (2023) does not appear when comparing sub-surface horizontal divergence to surface dimple count in the present study. This discrepancy may be partly methodological: in the current analysis, divergence is computed at a sub-surface plane approximately two viscous layers below the surface, whereas the cited study evaluates surface divergence directly. Additionally, the work of Babiker et al. (2023) is based on direct numerical simu-

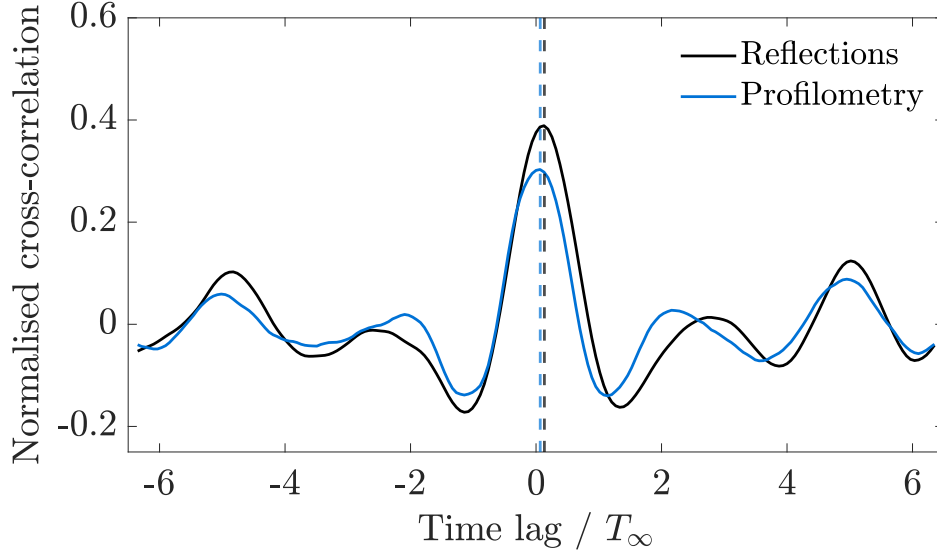


Figure 4.15: Normalised cross-correlation between dimple detections, from both profilometry and surface reflection detections, and the mean square horizontal divergence, plotted as a function of the time lag. The dashed lines correspond to the peak of the correlation function for each dataset.

lations (DNS) without a mean flow, while the present study relies on experimental data with a mean flow.

On a more speculative note, it could be hypothesised that the surface divergence associated with upwelling boils communicates downward through the fluid via pressure adjustments and inertia. As a result, the mean square horizontal divergence at a depth of approximately $2L_v$ may lag the surface divergence such that the peaks in horizontal divergence are captured almost simultaneously with dimple formation at the surface. This could explain why this lag is not present in the current analysis and also raises an intriguing question, easily addressable using DNS data for a future study: How does the lag between dimple count at the free surface and mean square horizontal divergence evolve as a function of depth?

Another plausible explanation for the absence of a significant lag between dimple count and divergence could be the effect of mean flow advection, as discussed above. The mean flow may carry the dimples out of the field of view before they are detected. If unrelated dimples from upstream upwellings are also advected into the field of view, this likely skews the correlation between divergence and dimple count.

Despite the various sources of uncertainty discussed throughout this chapter, the findings highlight the remarkable potential of using surface reflections to infer sub-surface flow dynamics. The reflection-based dimple detections exhibit a correlation with sub-surface horizontal divergence that is at least as strong and, in some respects, even more robust than the correlation observed using direct profilometry. This underlines the value of such simple reflection-based methods as a viable and potentially powerful tool for investigating near-surface turbulence.

4.6 Outlook and future directions

Due to the proof-of-concept nature of this study, one of the objectives outlined in Section 1.4 was to serve as a stepping stone for future studies on surface reflections and sub-surface turbulence. While some insights have been mentioned throughout Chapter 4, this section consolidates and discusses key takeaways to inform future research efforts.

For replications of the simultaneous acquisition of SPIV, profilometry, and surface reflections, several improvements can significantly streamline the post-processing and calibration required for the surface reflection recordings. The presence of green laser light in the acquisition process prevents perfect synchronisation between all three datasets, a problem that is likely difficult to overcome. However, the small mismatches in timestamps are relatively simple to account for. However, the mismatch in acquisition rates introduced a temporal drift in the reflection video, which left parts of the recording unusable. Aligned framerates throughout all measurements will significantly reduce the post-processing needs for a future study. Another suggested improvement is to project the physical coordinates onto the projector screen using calibration images, thereby eliminating the need for the manual calibration approach used in this project. Additionally, as discussed in Section 4.3, optimising the distance from the surface to the projector screen could improve the robustness of dimple detections and possibly reduce the number of false positives.

Several opportunities exist to further improve the wavelet-based detection method presented in this work. The current approach demonstrates how valuable information can be extracted from surface reflections and profilometry using readily available mathematical tools combined with key physical principles and straightforward reasoning about turbulence-surface interactions. Some minor improvements could potentially be achieved by delving more deeply into the choice of wavelet parameters, as discussed in Section 4.2.1. For engineering applications, more advanced object detection could be achieved by employing machine learning techniques. However, as initially stated in Section 1.4, one of the objectives of the project was to demonstrate how a simple method could provide significant insights without relying on complex algorithms. This transparency can simplify the interpretation of the underlying physics without requiring a detailed examination of the underlying methods.

This study focuses on a single dataset and its related flow conditions. A natural extension of this work would be to apply the same methodology to a broader range of flow conditions, including different Reynolds numbers, Froude numbers, Weber numbers and flow geometries. Furthermore, expanding the analysis to include additional surface features, such as scars, as explored by Aarnes et al. (2025), also provides a natural way forward for the proposed method for analysing surface reflections.

Related to loftier quests in terms of remote sensing and flow reconstructions, several interesting directions spring out of this work. One intriguing direction is the potential to reconstruct the full surface elevation profile using the surface reflection video. Achieving this would open up exciting possibilities for non-contact, image-based surface reconstruction techniques. While technically challenging, some opportunities are discussed in Section 2.5. Related approaches have been explored

by Dolcetti et al. (2021), who investigate surface reconstruction using acoustic methods.

Another interesting path forward is to use the reflected surface to infer and reconstruct the sub-surface flow field. Using the known physical principles alongside the detection and tracking of interesting structures could pave the way forward for utilising the SHRED framework proposed by Williams et al. (2024), which employs sparse sensors to reconstruct flow fields.

Chapter 5

Conclusions

This thesis presents a proof-of-concept study exploring the use of optical reflections from a free surface as a means to investigate sub-surface flow dynamics. Building on the understanding of how near-surface turbulence influences the free surface, the study aims to address three primary research questions: Is it possible to identify and track the imprints of surface-attached vortices, called dimples, through the optical reflections from a free surface; do these detected dimples correlate with sub-surface vortices and horizontal divergence; and how does this dimple detection method compare to direct surface elevation measurements using Fourier transform profilometry?

The wavelet-based computer vision method developed in this work successfully detects circular indentations on the free surface, provided that appropriate wavelet parameters are chosen. Because the method can track these structures in time, the shortest-lived detections, which are related to noise, can be filtered out, thereby enhancing the robustness of the dimple tracking. However, since the distance between the surface and the detector is fixed and may not align with the average focal plane of the dimples, there is some uncertainty regarding whether all dimples are reliably detected. This limitation highlights a potential area for improvement in future replications of these experiments.

Despite some limitations, the analysis demonstrates a significantly higher correspondence between surface detections and underlying vortices than what is expected from a random search, indicating that dimples are correctly identified. The match ratio, defined as the number of dimples with a vortex underneath divided by the total number of detected dimples, is lower than the values reported in previous studies using direct numerical simulations and a similar wavelet-based detection method. However, given that this study used experimental data, a different flow case and is subject to both spatial and temporal calibration uncertainties, this discrepancy is not unexpected. The match ratio for the reflection data is also lower than that obtained with profilometry, but these values are of comparable magnitude. Due to the high levels of noise in the profilometry, significantly fewer dimples are observed, with many dimples lost in the noise. This likely inflates the match ratio artificially for the profilometry data, as only the most pronounced detections are retained. This may indicate that the match ratios for profilometry and reflection detections are closer than the reported values suggest.

An interesting finding is that filtering the sub-surface vortices for a minimum lifetime, in the same manner as the dimples, has only a minor effect on the match

ratios. This process removes many short-lived vortices, leading to a more pronounced difference between the observed match ratios and those expected from a random search. Given that the sub-surface velocity field is derived from experimental data, this filtering is justified both as a means of reducing falsely identified vortices due to noise and to focus the analysis on the longest-lived and presumably strongest vortex structures.

A clear relationship is observed between the number of dimples detected in the surface reflections and the mean square horizontal divergence at a depth of $d = 10$ mm, which corresponds to approximately two viscous layer depths. In this analysis, the number of dimples detected in the surface reflection data yields a higher peak in the normalised cross-correlation than that of the profilometry data. Both datasets follow the mean square horizontal divergence with a minimal time lag, contrasting with earlier observations in direct numerical simulation data, where dimples are shown to lag behind surface divergence. The key distinction in the present study is that horizontal divergence is measured at a depth, not at the surface. A possible explanation for the time lag difference is that horizontal divergence in the sub-surface plane lags behind surface divergence, and this lag may be what is observed in the current results. Some of the time lag difference can also be attributed to calibration uncertainties. A final important note is that the present study differs in that a mean flow is present in these experiments. As a result, if dimples lag surface renewal, they may be advected out of the field of view before they appear.

In conclusion, this thesis introduces a simple, cost-efficient and physically interpretable method for detecting surface-attached vorticity by analysing optical reflections from a free surface. The detected surface features are shown to correlate with sub-surface turbulent structures and perform comparably to existing state-of-the-art methods. While the results are subject to certain limitations and uncertainties, these can easily be addressed in future research. By pursuing the proposed research directions, future studies and practical applications can continue to advance the understanding of free surface turbulence, simply by looking up at the ceiling.

References

- Aarnes, J. R., Babiker, O. M., Xuan, A., Shen, L., & Ellingsen, S. Å. (2025). Vortex structures under dimples and scars in turbulent free-surface flows. *Journal of Fluid Mechanics*, 1007, A38.
- Antoine, J.-P., Murenzi, R., Vandergheynst, P., & Ali, S. T. (2004). *Two-dimensional wavelets and their relatives* (1st ed.). Cambridge University Press.
- Babiker, O. M., Bjerkebæk, I., Xuan, A., Shen, L., & Ellingsen, S. Å. (2023). Vortex imprints on a free surface as proxy for surface divergence. *Journal of Fluid Mechanics*, 964, R2.
- Banerjee, S. (1994). Upwellings, downdrafts, and whirlpools: Dominant structures in free surface turbulence. *Applied Mechanics Reviews*, 47(6S), S166–S172.
- Brinkerhoff, C. B., Gleason, C. J., Zappa, C. J., Raymond, P. A., & Harlan, M. E. (2022). Remotely sensing river greenhouse gas exchange velocity using the swot satellite. *Global Biogeochemical Cycles*, 36(10).
- Brocchini, M., & Peregrine, D. H. (2001). The dynamics of strong turbulence at free surfaces. part 1. description. *Journal of Fluid Mechanics*, 449, 225–254.
- Brumley, B. H., & Jirka, G. H. (1987). Near-surface turbulence in a grid-stirred tank. *Journal of Fluid Mechanics*, 183, 235–263.
- Brunton, S. L., & Kutz, J. N. (2019). *Data-driven science and engineering: Machine learning, dynamical systems, and control*. Cambridge University Press.
- D'Asaro, E. A. (2014). Turbulence in the upper-ocean mixed layer. *Annual Review of Marine Science*, 6(Volume 6, 2014), 101–115.
- Dolcetti, G., Alkmim, M., Cuenca, J., De Ryck, L., & Krynnin, A. (2021). Robust reconstruction of scattering surfaces using a linear microphone array. *Journal of Sound and Vibration*, 494, 115902.
- Dolcetti, G., Hortobágyi, B., Perks, M., Tait, S. J., & Dervilis, N. (2022). Using noncontact measurement of water surface dynamics to estimate river discharge. *Water Resources Research*, 58(9), e2022WR032829.
- Dolcetti, G., & Nava, H. G. (2019). Wavelet spectral analysis of the free surface of turbulent flows. *Journal of Hydraulic Research*, 57(2), 211–226.
- Farge, M. (1992). Wavelet transforms and their applications to turbulence. *Annual Review of Fluid Mechanics*, 24(Volume 24, 1992), 395–458.
- Foreman, J., J. W., George, E. W., & Lewis, R. D. (1965). Measurement of localized flow velocities in gases with a laser doppler flowmeter. *Applied Physics Letters*, 7(4), 77–78.
- Fuchs, A., Kharche, S., Patil, A., Friedrich, J., Wächter, M., & Peinke, J. (2022). An open source package to perform basic and advanced statistical analysis of turbulence data and other complex systems. *Physics of Fluids*, 34(10), 101801.

- Gakhar, S., Koseff, J., & Ouellette, N. (2022). Extracting free-surface expressions of underwater features. *Experiments in Fluids*, 63.
- Gao, M. L., Williams, J. P., & Kutz, J. N. (2025). Sparse identification of nonlinear dynamics and Koopman operators with shallow recurrent decoder networks [arXiv preprint: <https://arxiv.org/abs/2501.13329>].
- Griffiths, D. (2013). *Introduction to electrodynamics* (4th ed.). Pearson.
- Grossmann, A. (1988). Wavelet transforms and edge detection. In S. Albeverio, P. Blanchard, M. Hazewinkel, & L. Streit (Eds.), *Stochastic processes in physics and engineering* (pp. 149–157). Springer Netherlands.
- Guo, X., & Shen, L. (2010). Interaction of a deformable free surface with statistically steady homogeneous turbulence. *Journal of Fluid Mechanics*, 658, 33–62.
- Heisenberg, W. (1927). Über den anschaulichen Inhalt der quantentheoretischen Kinematik und Mechanik. *Zeitschrift für Physik*, 43(3-4), 172–198.
- Herlina, H., & Jirka, G. H. (2008). Experiments on gas transfer at the air–water interface induced by oscillating grid turbulence. *Journal of Fluid Mechanics*, 594, 183–208.
- Herlina, H., & Wissink, J. G. (2014). Direct numerical simulation of turbulent scalar transport across a flat surface. *Journal of Fluid Mechanics*, 744, 217–249.
- In, F., & Kim, S. (2012). *An introduction to wavelet theory in finance*. World Scientific.
- Jeong, J., & Hussain, F. (1995). On the identification of a vortex. *Journal of Fluid Mechanics*, 285, 69–94.
- Jooss, Y., Li, L., Bracchi, T., & Hearst, R. J. (2021). Spatial development of a turbulent boundary layer subjected to freestream turbulence. *Journal of Fluid Mechanics*, 911.
- Kermani, A., & Shen, L. (2009). Surface age of surface renewal in turbulent interfacial transport. *Geophysical Research Letters*, 36(10).
- Kolmogorov, A. (1941). The local structure of turbulence in incompressible viscous fluid for very large Reynolds' numbers. *Akademiiia Nauk SSSR Doklady*, 30, 301–305.
- Kundu, P., & Cohen, I. (2012). *Fluid mechanics* (5th ed.). Academic Press.
- Li, L., Bullee, P. A., Ellingsen, S. Å., & Hearst, R. J. (2025). Sub-surface turbulence or non-breaking capillary waves: Which dominates air–water gas transfer? *Journal of Fluid Mechanics*, 1009, A48.
- Magnaudec, J. (2003). High-reynolds-number turbulence in a shear-free boundary layer: Revisiting the Hunt–Graham theory. *Journal of Fluid Mechanics*, 484, 167–196.
- Mallat, S. (1999). *A wavelet tour of signal processing* (2nd ed.). Academic press.
- Mandel, T. L., Gakhar, S., Chung, H., Rosenzweig, I., & Koseff, J. R. (2019). On the surface expression of a canopy-generated shear instability. *Journal of Fluid Mechanics*, 867, 633–660.
- Martens Meyer, H. (2024). Analysis of free-surface fluid flows of increasing complexity using data-driven methods [Unpublished specialization project].
- MathWorks. (2024). *Wavelet toolbox version: 24.2 (r2024b)*. Natick, Massachusetts, United States.

- McKenna, S., & McGillis, W. (2004). The role of free-surface turbulence and surfactants in air–water gas transfer. *International Journal of Heat and Mass Transfer*, 47(3), 539–553.
- Muraro, F., Dolcetti, G., Nichols, A., Tait, S. J., & Horoshenkov, K. V. (2021). Free-surface behaviour of shallow turbulent flows. *Journal of Hydraulic Research*, 59, 1–20.
- Nobach, H., Müller, E., & Tropea, C. (1998). Efficient estimation of power spectral density from laser Doppler anemometer data. *Experiments in Fluids*, 24, 499–509.
- Pope, S. B. (2000). *Turbulent flows*. Cambridge University Press.
- Prasad, A. (2000). Stereoscopic particle image velocimetry. *Experiments in Fluids*, 29, 103–116.
- Reynolds, O. (1895). IV. On the dynamical theory of incompressible viscous fluids and the determination of the criterion. *Philosophical Transactions of the Royal Society of London. (A.)*, 186, 123–164.
- Richardson, L. F. (1922). *Weather prediction by numerical process*. Cambridge University Press.
- Rocher-Ros, G., Sponseller, R. A., Lidberg, W., Mört, C.-M., & Giesler, R. (2019). Landscape process domains drive patterns of CO₂ evasion from river networks. *Limnology and Oceanography Letters*, 4(4), 87–95.
- Savelsberg, R., Holten, A., & van de Water, W. (2006). Measurement of the gradient field of a turbulent free surface. *Experiments in Fluids*, 41(4), 629–640.
- Scardovelli, R., & Zaleski, S. (1999). Direct numerical simulation of free-surface and interfacial flow. *Annual Review of Fluid Mechanics*, 31, 567–603.
- Schlichting, H., & Gersten, K. (2016). *Boundary-layer theory* (9th ed.). Springer Berlin Heidelberg.
- Schram, C., Rambaud, P., & Riethmüller, M. L. (2004). Wavelet based eddy structure eduction from a backward facing step flow investigated using particle image velocimetry. *Experiments in Fluids*, 36, 233–245.
- Shen, L., Zhang, X., Yue, D. K. P., & Triantafyllou, G. S. (1999). The surface layer for free-surface turbulent flows. *Journal of Fluid Mechanics*, 386, 167–212.
- Simonsen, V. P., Bedeaux, D., & Simonsen, I. (2021). Nonparametric reconstruction of the statistical properties of penetrable, isotropic randomly rough surfaces from in-plane, co-polarized light scattering data: Application to computer-generated and experimental scattering data. *Phys. Rev. A*, 104, 043502.
- Su, X., & Chen, W. (2001). Fourier transform profilometry: A review. *Optics and Lasers in Engineering*, 35(5), 263–284.
- Su, Y., Tan, W., Dong, Y., Xu, W., Huang, P., Zhang, J., & Zhang, D. (2024). Enhancing concealed object detection in active millimeter wave images using wavelet transform. *Signal Processing*, 216, 109303.
- Taylor, G. I. (1935). Statistical theory of turbulence. *Proceedings of the Royal Society of London. Series A, Mathematical and Physical Sciences*, 151(873), 421–444.
- Taylor, G. I. (1938). The spectrum of turbulence. *Proceedings of the Royal Society of London. Series A - Mathematical and Physical Sciences*, 164(919), 476–490.

- Tennekes, H., & Lumley, J. (1972). *A first course in turbulence*. MIT Press.
- Veron, F., Melville, W. K., & Lenain, L. (2011). The effects of small-scale turbulence on air-sea heat flux. *Journal of Physical Oceanography*, 41(1), 205–220.
- Wang, N., & Lu, C. (2010). Two-dimensional continuous wavelet analysis and its application to meteorological data. *Journal of Atmospheric and Oceanic Technology*, 27(4), 652–666.
- Wanninkhof, R., Asher, W., Ho, D., Sweeney, C., & McGillis, W. (2009). Advances in quantifying air-sea gas exchange and environmental forcing. *Annual review of marine science*, 1, 213–44.
- Williams, J. P., Zahn, O., & Kutz, J. N. (2024). Sensing with shallow recurrent decoder networks. *Proceedings of the Royal Society A: Mathematical, Physical and Engineering Sciences*, 480(2298), 20240054.
- Yeh, Y., & Cummins, H. Z. (1964). Localized fluid flow measurements with an He-Ne laser spectrometer. *Applied Physics Letters*, 4(10), 176–178.

Appendix

A Code availability

The code developed and used throughout this project is available on <https://github.com/hmartensmeyer>.

